



Publication Year	2022
Acceptance in OA@INAF	2022-09-02T10:19:05Z
Title	þ The REACH radiometer for detecting the 21-cm hydrogen þ 7.5 28
Authors	de Lera Acedo, E.; de Villiers, D. I.L.; Razavi-Ghods, N.; Handley, W.; Fialkov, A.; et al.
DOI	10.1038/s41550-022-01709-9
Handle	http://hdl.handle.net/20.500.12386/32546
Journal	NATURE ASTRONOMY



The REACH radiometer for detecting the 21-cm hydrogen signal from redshift $z \approx 7.5$ –28

E. de Lera Acedo ^{1,2} , D. I. L. de Villiers ³, N. Razavi-Ghods¹, W. Handley ^{1,2}, A. Fialkov ^{2,4}, A. Magro ⁵, D. Anstey¹, H. T. J. Bevens ¹, R. Chiello⁶, J. Cumner¹, A. T. Josaitis¹, I. L. V. Roque ¹, P. H. Sims ^{7,8}, K. H. Scheutwinkel ¹, P. Alexander¹, G. Bernardi^{9,10,11}, S. Carey¹, J. Cavillot¹², W. Croukamp³, J. A. Ely¹, T. Gessey-Jones ¹, Q. Gueuning¹, R. Hills ^{1,20}, G. Kulkarni ¹³, R. Maiolino^{1,2}, P. D. Meerburg¹⁴, S. Mittal ¹³, J. R. Pritchard¹⁵, E. Puchwein¹⁶, A. Saxena ¹⁴, E. Shen¹, O. Smirnov ^{10,11}, M. Spinelli ^{17,18,19} and K. Zarb-Adami^{5,6}

Observations of the 21-cm line from primordial hydrogen promise to be one of the best tools to study the early epochs of the Universe: the dark ages, the cosmic dawn and the subsequent epoch of reionization. In 2018, the Experiment to Detect the Global Epoch of Reionization Signature (EDGES) caught the attention of the cosmology community with a potential detection of an absorption feature in the sky-averaged radio spectrum centred at 78 MHz. The feature is deeper than expected, and, if confirmed, would call for new physics. However, different groups have re-analysed the EDGES data and questioned the reliability of the signal. The Radio Experiment for the Analysis of Cosmic Hydrogen (REACH) is a sky-averaged 21-cm experiment aiming at improving the current observations by tackling the issues faced by current instruments related to residual systematic signals in the data. The novel experimental approach focuses on detecting and jointly explaining these systematics together with the foregrounds and the cosmological signal using Bayesian statistics. To achieve this, REACH features simultaneous observations with two different antennas, an ultra-wideband system (redshift range about 7.5 to 28) and a receiver calibrator based on in-field measurements. Simulated observations forecast percent-level constraints on astrophysical parameters, potentially opening up a new window to the infant Universe.

The first stars and galaxies formed some time after the epoch of recombination, when the cosmic microwave background (CMB) decoupled $\sim 378,000$ years after the Big Bang at a redshift (z) of $\sim 1,100$, and before the current ‘realm of galaxies’ that we can see today^{1–3}. The radiation from these first luminous sources heated and reionized the neutral hydrogen that pervaded the primordial cosmos^{2,4}. Probing the intermediate epochs, the ‘dark ages’ before the first stars through first new light in the Universe and cosmic reionization, represents a frontier in the study of cosmic structure formation^{5,6}. The hyperfine transition of neutral hydrogen has a restframe wavelength of 21 cm and by observing at low radio frequencies we can directly study its redshifted radio emission (and absorption) from the gas clouds that were the raw material that formed the first luminous cosmic structures at these early epochs^{4–6}. Figure 1 shows an example of the sky-averaged (global) 21-cm signal for an assumed succession of cosmic events. However, as high-redshift models are poorly constrained by existing data, a large variety of 21-cm signals are still plausible and the timing and order of cosmic events is not well understood^{7–10}.

A number of experiments to measure the global redshifted 21-cm signal are already underway, including the Experiment to Detect the Global Epoch of Reionization Signature (EDGES)¹¹, Shaped Antenna Measurement of the Background Radio Spectrum (SARAS)¹², Probing Radio Intensity at High-Z from Marion (PRIZM)¹³, the Large-Aperture Experiment to Detect the Dark Ages (LEDA)¹⁴ and the Sonda Cosmológica de las Islas para la Detección de Hidrógeno Neutro (SCI-H I)¹⁵, have reported results in the recent years, such as the Broadband Instrument for Global Hydrogen Reionisation Signal (BIGHORNS)¹⁶, or are being planned, such as the Dark Ages Polarimeter Pathfinder (DAPPER; <https://www.colorado.edu/project/dark-ages-polarimeter-pathfinder/>) and the Mapper of the IGM Spin Temperature (MIST; <http://www.physics.mcgill.ca/mist/>), among others. The deep absorption profile recently detected by the EDGES collaboration at a frequency of 78 MHz (ref. 17) is the first candidate detection of the global 21-cm signal from $z \approx 17$. If truly of cosmological origin, as opposed to being caused by instrumental systematical errors or by foreground signals, this signal implies notable star formation at high redshifts^{9,10,18,19} and,

¹Cavendish Astrophysics, University of Cambridge, Cambridge, UK. ²Kavli Institute for Cosmology in Cambridge, University of Cambridge, Cambridge, UK. ³Department of Electrical and Electronic Engineering, Stellenbosch University, Stellenbosch, South Africa. ⁴Institute of Astronomy, University of Cambridge, Cambridge, UK. ⁵Institute of Space Sciences and Astronomy, University of Malta, Msida, Malta. ⁶Physics Department, University of Oxford, Oxford, UK. ⁷McGill Space Institute, McGill University, Montreal, Quebec, Canada. ⁸Department of Physics, McGill University, Montreal, Quebec, Canada. ⁹INAF—Istituto di Radio Astronomia, Bologna, Italy. ¹⁰Department of Physics and Electronics, Rhodes University, Grahamstown, South Africa. ¹¹South African Radio Astronomy Observatory, Cape Town, South Africa. ¹²Antenna Group, Université catholique de Louvain, Louvain, Belgium. ¹³Department of Theoretical Physics, Tata Institute of Fundamental Research, Mumbai, India. ¹⁴Faculty of Science and Engineering, University of Groningen, Groningen, The Netherlands. ¹⁵Department of Physics, Imperial College London, London, UK. ¹⁶Leibniz Institute for Astrophysics, Potsdam, Germany. ¹⁷INAF—Osservatorio Astronomico di Trieste, Trieste, Italy. ¹⁸IFPU—Institute for Fundamental Physics of the Universe, Trieste, Italy. ¹⁹Department of Physics and Astronomy, University of the Western Cape, Bellville, South Africa. ²⁰Deceased: R. Hills. e-mail: eloy@mrao.cam.ac.uk

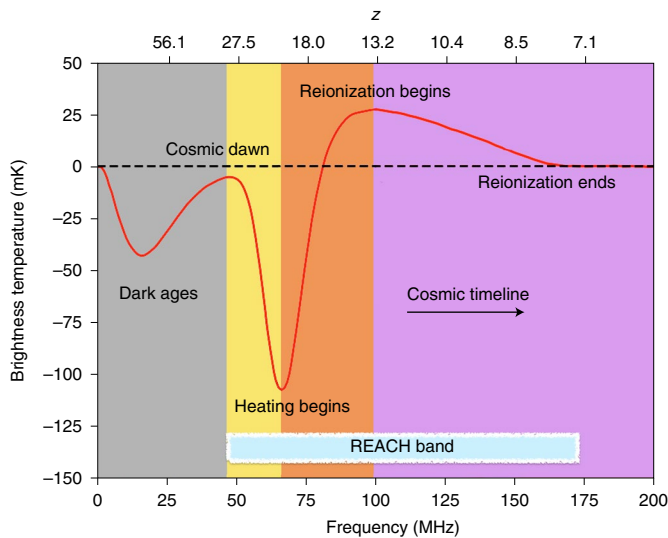


Fig. 1 | A typical model of the global 21-cm line. Main cosmic events are highlighted^{23,24}. From left to right: collisional coupling (grey), onset of Ly- α coupling (yellow), onset of X-ray heating (orange), photoionization (purple). REACH will explore the frequency range 50–170 MHz ($z \approx 7.5$ –28).

thus, could be real evidence of the primordial population of stars. However, the amplitude of the detected signal of 500^{+500}_{-200} mK (at 99% confidence) is too strong compared with the standard expectations obtained with conventional astrophysical modelling^{20–22}. The standard scenario^{23,24} assumes that the atomic hydrogen gas is first cooled down by the expansion of the Universe to temperatures well below that of the CMB and then heated by X-ray sources. Lyman- α (Ly- α) photons produced by the first population of stars couple the 21-cm spin temperature to the kinetic temperature of the gas, thus rendering the 21-cm signal visible against the background radiation via the process called Wouthuysen–Field coupling^{25,26}. It is standard practice to assume that the 21-cm signal is observed against the CMB, and in this picture the depth of the absorption trough is at most ~ 200 mK at $z \approx 17$ (ref. ⁹), with the deepest features achieved assuming saturated Wouthuysen–Field coupling and gas cooled by the adiabatic expansion of the Universe in the absence of X-ray (or other) heating sources. If not explained by hardware systematics, the anomalously deep feature reported by EDGES calls for exotic theoretical interpretations (see more in the ‘Exotic interpretations of the EDGES signal’ section in the Methods).

The Radio Experiment for the Analysis of Cosmic Hydrogen (REACH), introduced in this work, was proposed to independently measure the high-redshift 21-cm signal in the $\nu = 50$ –170 MHz frequency range ($z \approx 7.5$ –28), and thus either verify or disprove the EDGES detection. The REACH pipeline will include a variety of theoretical models (both standard and exotic). If a cosmological 21-cm signal is detected, these models will allow us to measure/constrain astrophysical parameters associated with primordial star and black hole formation, thermal and ionization histories of the Universe and radio production efficiency of high-redshift astrophysical sources. Specifically, the location and depth of the absorption trough in the 21-cm signal can tell us: (1) the timing of primordial star formation, (2) the properties of the first star-forming objects (mass and star-formation efficiency) and (3) the luminosity of the first X-ray sources (for example, the first population of X-ray binaries). REACH will also be able to tell us whether the standard astrophysical picture has to be revised by, for instance, adding an excess radio background and/or extra cooling at high redshifts. In the case of a non-detection, the upper limits on the strength of the

absorption feature within the REACH frequency band can be used to bound high-redshift astrophysics. Low-intensity signals within the REACH band would require either the X-ray sources to be very luminous or for star formation to happen very late and in very massive dark matter halos. In addition, models that assume extreme radio background and/or dark matter overcooling would be considered less likely.

Re-analysis of public EDGES data has resulted in concerns about the data analysis presented by EDGES, which uses a fit with a basic foreground model with non-physical parameters²⁷. Recent studies^{28–30} have also revealed alternative ways of explaining the data in terms of residual instrumental systematics, as shown in Extended Data Fig. 1 and described with more detail in the ‘EDGES data re-analysis’ section in the Methods. Recently, the SARAS collaboration has published an analysis of data collected with their latest antenna design (a monocone antenna floating on lake water) showing residuals incompatible with the cosmological signal profile reported by EDGES³¹.

To solve this puzzle and aim at a confident detection of the 21-cm signal, REACH has been designed to avoid systematic signals potentially degenerate with the cosmological signal and to detect any residual systematic signals and model them in the data together with the cosmological fits. This is achieved by using physically based foreground and instrument models that will be jointly fitted, using Bayesian inference, with the cosmic signal models. The aim of this approach is to be able to explain any residual instrument systematics and their correlation with the foregrounds and cosmological signals. In the presence of unaccounted systematics, techniques have been developed using maximally smooth functions (MSFs) for their identification and mathematical characterization. This is in contrast with the first-generation sky-averaged experiments (for example, refs. ^{11,12}), where the main focus was on developing and operating an instrument that was as achromatic (spectrally smooth) as possible. A summary table comparing the main experimental features of existing experiments with REACH is shown in Table 1. REACH, to our best knowledge, is the only ground-based 21-cm global experiment featuring a full joint Bayesian model fitting including all signal components.

REACH is a wideband experiment covering both the cosmic dawn and the epoch of reionization. REACH will use a nested sampling tool, PolyChord^{32,33}, and parametric foreground, instrument and 21-cm signal models²⁰ for the signal detection. REACH also features a switched calibrator radio-frequency (RF) receiver using in-field measurements of the analogue and digital components on the receiving chain. The calibration of the receiver uses a fast Bayesian conjugate-prior-based approach. REACH Phase I is currently being deployed in the radio-frequency interference (RFI)-quiet Karoo radio reserve in South Africa, which is the location of the Hydrogen Epoch of Reionization Array (HERA), MeerKAT and future Square Kilometre Array (SKA)1-Mid experiments^{34–36}. REACH Phase I will observe the sky with two independent and different antennas simultaneously. The antenna designs (a conical log-spiral antenna and a hexagonal dipole) have been selected using a simulated pipeline and maximizing the Bayesian log evidence for an assumed 21-cm signal model in the received data while minimizing the error in the recovered 21-cm signal. More details of this are provided in the Methods. This paper introduces the experiment: the methodology and experimental approach as well as a brief description of its hardware and software (algorithm) components. As the project evolves and we analyse real sky data and laboratory measurements, we expect to validate the approach described here as well as to find that modifications of the different components may be required. A series of papers authored by members of the REACH team describing different components of the experiment in more detail are publicly available. These are referred to throughout the text and include: the description of the

Table 1 | Comparison of main experimental features of existing global experiments with REACH

Experiment	Bandwidth	Frequency band (MHz)	Simultaneous observations	Antenna type	Receiver calibrator and spectrometer	Full Bayesian analysis
EDGES	2:1	50–100 (Low band), 100–200 (High band)	No	Blade dipole	Lab measurements, auto-correlation	No
SARAS	5:1	40–200 (SARAS2)	No	Monopole	Lab measurements, cross-correlation	No
LEDA	2.125:1	30–85	No	Crossed drooping dipole	Lab measurements, auto-correlation	No
PRIZM	2:1	50–90, 70–140	No	Crossed-dipole (four-square)	Lab measurements, auto-correlation	No
SCI-HI	3.21:1	40–130	No	HIBiscus	Lab measurements, auto-correlation	No
BIGHORNS	2.85:1	70–200	No	Conical log-spiral	Lab measurements, auto-correlation	No
REACH	3.4:1	50–170	2 antennas	Hexagonal dipole, Conical log-spiral	In-field measurements, auto-correlation	Yes

Bayesian data analysis pipeline³⁷, the description of the Bayesian receiver calibration³⁸, the antenna selection using the Bayesian data pipeline³⁹, the design of the Phase I wideband dipole⁴⁰, the assessment of ionospheric effects⁴¹, the detection of systematic signals using MSFs³⁰, the sky-averaged 21-cm signal emulator⁴², the Bayesian evidence-driven likelihood selection⁴³ and the Bayesian evidence-driven diagnosis of instrumental systematics⁴⁴.

REACH is planned to be staged in phases. A Phase II will follow featuring further antenna systems, which could include scaled versions of the Phase I antennas or complementary antenna systems sensitive to other polarizations of the sky radiation, amongst others.

In the section ‘Experimental approach’, we highlight and briefly discuss the main features of the REACH experiment. The section ‘System design’ depicts the high-level hardware design, later expanded on in the Methods section. The sections ‘Data analysis pipeline’ and ‘Science prospects’ describe the joint Bayesian data and science analysis pipeline and shows the predicted performance of REACH and its ability to constrain the relevant cosmological models based on a simulated data analysis. We conclude with some final remarks in the ‘Conclusion’ section and in the Methods section the main methods developed for REACH are explained.

Experimental approach

The novel experimental approach of REACH is focused on understanding and jointly constraining telescope systematics with the cosmological and foreground signal.

The spectral and spatial structure of the foregrounds couple with the spectral and spatial variations of the antenna on the ground, resulting (even for a simple dipole antenna) in antenna temperature variations that cannot be modelled with a simple low-order polynomial and that are highly dependent on local sidereal time and integration times. Reflections and spectral features in the analogue receiver can also have scales similar to those of the target cosmological signal. If any such systematic feature remains in the data after calibration, it may not be possible to accurately constrain the cosmological models.

To achieve a convincing and confident detection of the 21-cm signal, we argue that the foreground models should be independent from the instrument models and the cosmological models, and that the correlation between their parameters needs to be clearly explained and isolated in the data analysis. This should also be done using physics-rooted models and field measurements and be supported by the robust statistical inference.

To achieve this, REACH uses a Bayesian calibration and data analysis pipeline where correlation between all the different parameters can be explained in a statistical manner. REACH has been designed to avoid instrumental systematic signals in the first place, but to deal with any residual systematic effects we have used a simulated version of the data pipeline to design an instrument where all three signal spaces (cosmological signal, foregrounds and instrument) are largely orthogonal³⁹. While this approach does not ensure success in achieving the very challenging detection, it provides a framework to enhance the robustness of the data analysis against the effect of instrumental systematic signals. This process, however, requires a substantial amount of information to constrain the models. To provide this extra information, in REACH Phase I we feature the following novelties, unique to this type of experiment.

Simultaneous observations with two different antennas. REACH will observe the Southern Hemisphere sky with two different radio antennas simultaneously. The data collected by the two antennas will then be analysed jointly to better understand and isolate signal components associated with the hardware systematics. The benefits of doing so are discussed in more detail in the ‘Time- and antenna-dependent modelling’ section in the Methods. These antennas are, for Phase I, a hexagonal dipole and a conical log-spiral antenna. In the ‘Antennas’ section in the Methods, we describe the design process for choosing antenna types and optimizing their performance. For Phase II we then expect to deploy further antennas, including scaled versions of the dipole and a dual polarization system. Furthermore, the use of two antennas, even if primarily used to analyse auto-correlated data, will allow us to cross correlate (in an interferometric sense) their output voltages to further constrain hardware systematics.

Ultra-wideband system. Separating the foregrounds from the cosmological 21-cm signal relies almost entirely on their different spectral components. The foregrounds, dominated by synchrotron radiation from our own galaxy, are expected to be smooth⁴⁵, well described by a power law in frequency. The sky-averaged 21-cm signal, however, as shown in Fig. 1, is expected to oscillate in frequency and exhibit 3 turning points between 50 MHz and 170 MHz. Thus, a larger frequency bandwidth should provide more chances to leverage these spectral differences. First-generation 21-cm global experiments^{46–48}, in contrast with the approach of REACH, rely almost entirely on the smoothness of the instrument response across frequencies to avoid introducing spectral components into

REACH Phase I system diagram

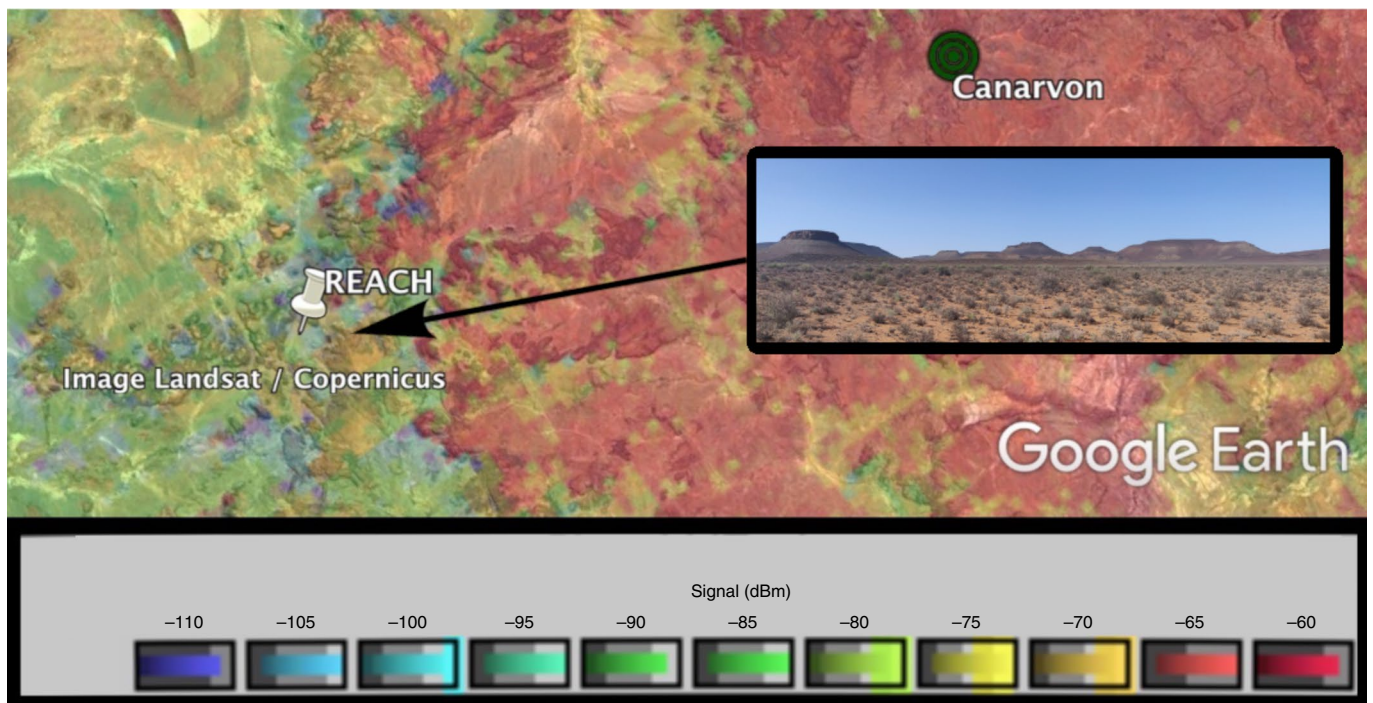
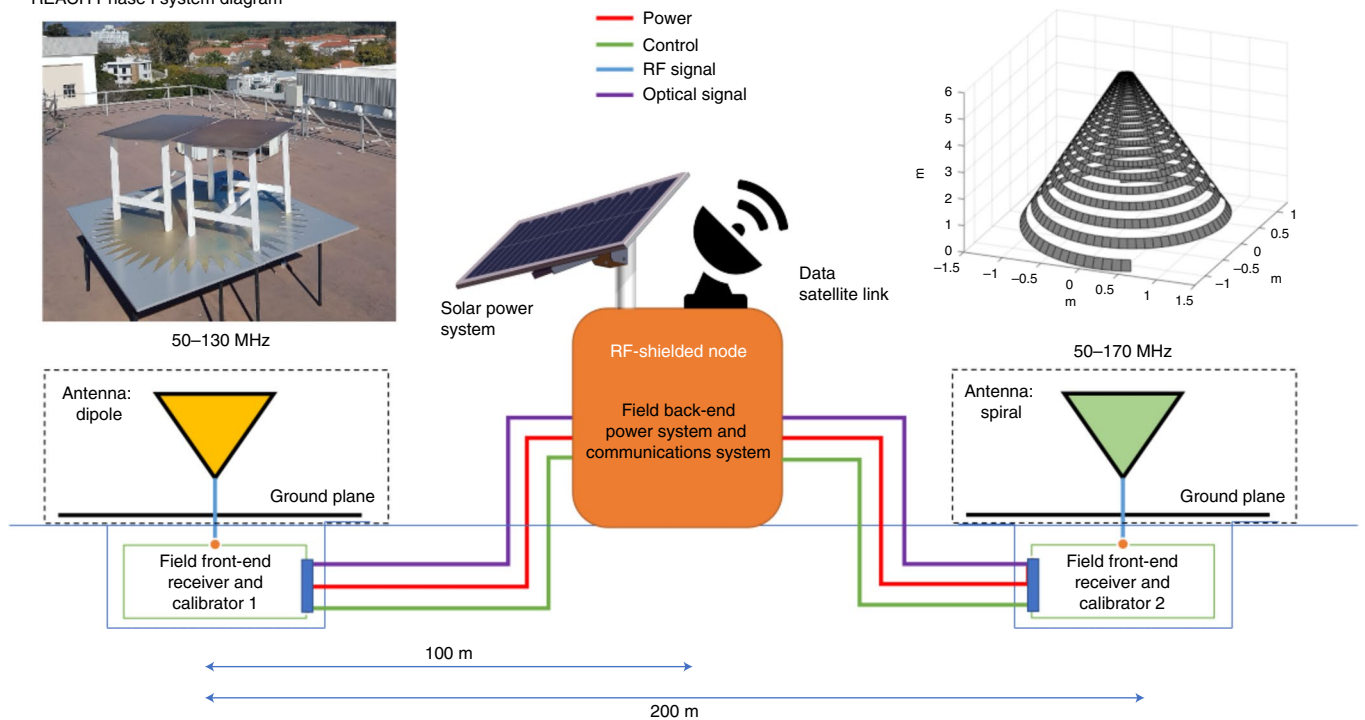


Fig. 2 | REACH Phase I field system and location. The top panel shows the REACH Phase I field system featuring two independent radiometers. The bottom panel shows an aerial satellite image of the REACH site where the different colours indicate the strength of the FM signal originating in Canarvon (www.peralex.com provided the FM radio survey data). A photo of the REACH site in the Great Karoo semi-desert in South Africa is shown in the small window. Bottom image from Google Earth based on Landsat/Copernicus surveys.

the foreground signals. Aiming at this instrument smoothness, EDGES restricted their frequency band to a bandwidth ratio of approximately 2:1 and operates scaled systems with a small overlapping band to cover the full frequency range. The joint statistical analysis approach used in REACH does not require that level of smoothness, and in some cases ('Foreground models and chromaticity correction' section in the Methods) certain frequency

structures in the system response may be preferred, and therefore larger instantaneous frequency bands can be accessed (up to $\sim 3.5:1$ with the conical log-spiral antenna).

Receiver calibration based on in-field measurements. Extensive work has been carried out by experiments like EDGES⁴⁹ to optimize the calibration of the receiver electronics by using a switched

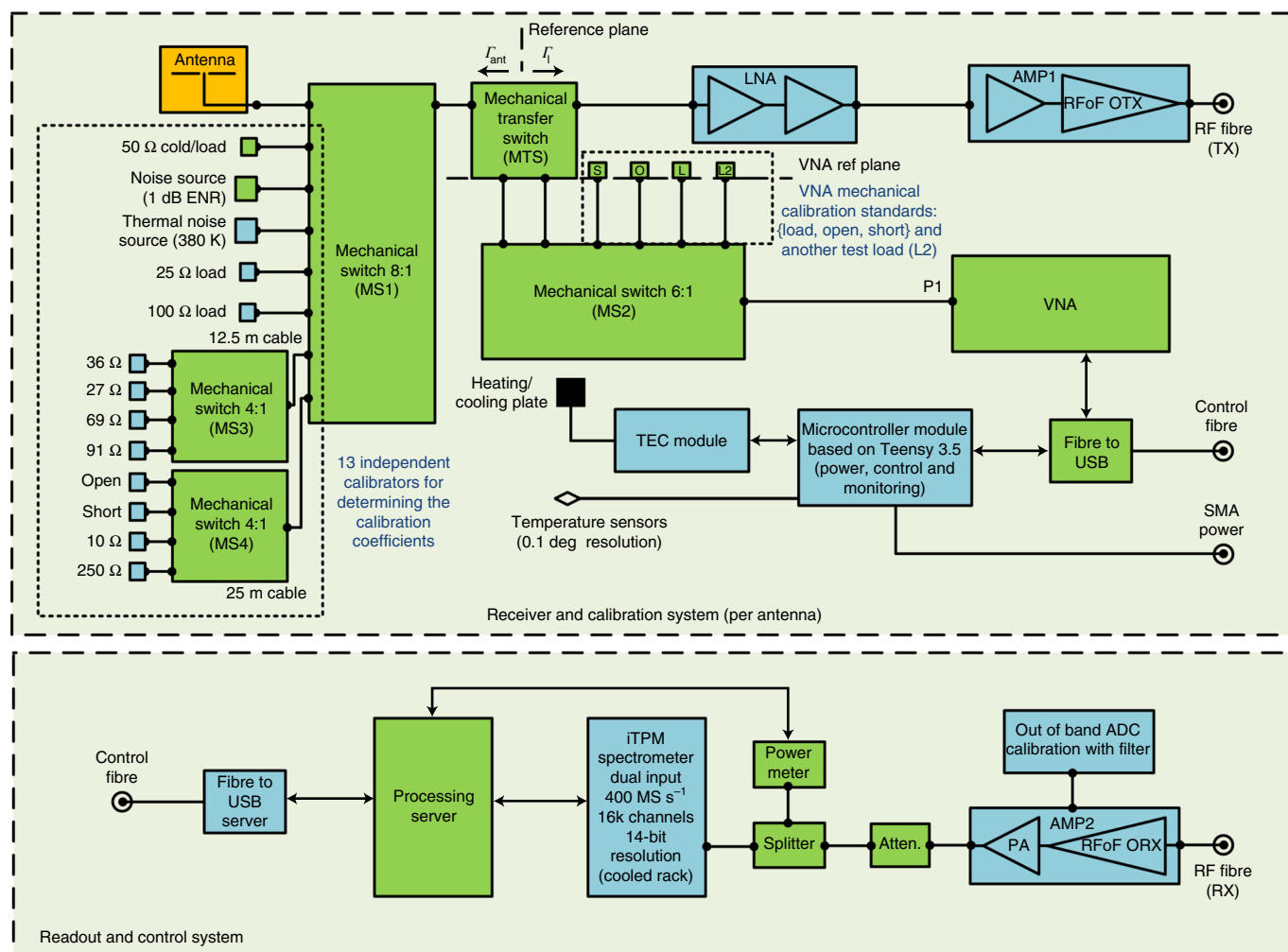


Fig. 3 | Field and back-end hardware diagram (per antenna). The exact value of the calibration sources (left of the figure, connected to the mechanical switches) varies depending on the antenna connected to the receiver. Green blocks represent off-the-shelf components, whilst blue are custom designs. Γ_{ant} is the reflection coefficient of the antenna; Γ_1 is the reflection coefficient of the LNA; 'ENR' is the Excess Noise Ratio; 'RFoF' stands for Radio Frequency over Fibre; 'OTX' indicates an optical transmitter; 'TX' indicates transmission mode; 'TEC' stands for Thermo Electric Cooling; 'SMA' is a SubMiniature version A connector; 'PA' is a Power Amplifier; 'RX' indicates reception mode and 'Atten.' represents a signal attenuator.

calibrator system. This calibration has so far relied on very meticulous and precise measurements of the different electronic components of the receiver in a well-controlled laboratory environment. However, once deployed, the time stability of the system and its sensitivity to environmental effects (for example, temperature) can translate into an inaccurate calibration. To overcome this, REACH features an in-field measurement system, using a compact vector network analyser (VNA) integrated with the receiver to provide real-time monitoring of the antenna and receiver components.

System design

In this section, we briefly describe the hardware system for REACH. Further information about the system and its location can be found in the Methods section.

In Fig. 2 we show a high-level overview of the field system, while Fig. 3 shows the details of the analogue and digital receivers, including the calibrator system. The 'Antennas' section in the Methods describes the antennas that will be used in Phase I.

The REACH Phase I field system features 2 independent radiometers with different antenna designs (a hexagonal dipole antenna (50–130 MHz) and a conical log-spiral antenna (50–170 MHz)), as shown in Fig. 2. REACH Phase I is a stand-alone instrument powered from a solar power system and connected to the world via an

internet satellite link. Its location in the Karoo semi-desert area of South Africa has been chosen based on several parameters including accessibility and low RFI. A radio propagation study, using the Longley–Rice propagation model, for total power in the FM band (88–108 MHz) radiated from the transmitter in Carnarvon across the topography of the Karoo Radio Astronomy Reserve is shown in Fig. 2. The RF receiver system, incorporating the aforementioned in-field calibrator, is followed by a high-resolution spectrometer featuring 6-kHz-wide channels (for RFI excision) and is based on the SKA1-Low Tile Processing Module (TPM) Field-programmable Gate Array (FPGA) board.

The 'Receiver and calibrator' section in the Methods explains the different hardware components in the analogue chain, including those used for its calibration. The 'Digital back-end' section in the Methods is a high-level overview of the digital high-resolution spectrometer used in REACH. In the 'Site and RFI' section in the Methods, we discuss the choice of location and the RFI environment. Finally, in the 'High-level system metrics' section in the Methods we summarize the main technical capabilities of REACH.

Data analysis pipeline

The data analysis pipeline for REACH Phase I is depicted in Fig. 4. After the receiver has been calibrated using in-field measurements

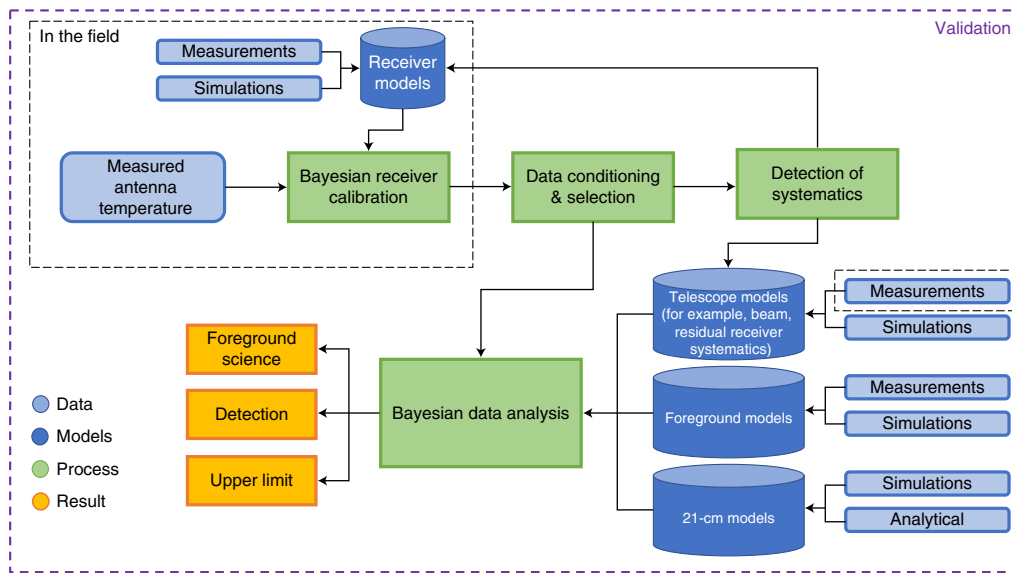


Fig. 4 | Data analysis and calibration diagram. The diagram depicts the data flow around the joint Bayesian model fitting at the heart of REACH. A pre-calibration step takes place in the field, where the receiver electronics are calibrated using a Bayesian calibrator and a set of in-field measurements. Following this step, the data are transferred off-site, where after a pre-selection of high-quality data we perform an analysis in search of unknown (for example, lacking a specific model) systematic signals remaining in the data. Finally, a joint model fitting process using Bayesian inference is performed on the data using pre-designed telescope, foreground and cosmological signal models. These models, specifically those associated with the telescope, will also be informed by direct measurements of, for example, the radio antenna.

(Extended Data Fig. 2 and the ‘Bayesian receiver calibration’ section in the Methods), a pre-processing step of high-quality data selection will be performed off-site (for example, data from nights with a quiet ionosphere). These data will then be analysed with a suite of tools to detect unknown systematic signals (‘Detection of systematic errors’ section in the Methods). The result of this analysis will help inform the pre-designed telescope (‘Instrument models’ section in the Methods), foreground (Extended Data Fig. 3 and ‘Foreground models and chromaticity correction’ section in the Methods) and cosmological (‘Cosmological models’ section in the Methods) models. For example, a potential outcome of the analysis of unknown systematic errors would be a new model component to capture this systematic signal. Then, the pre-calibrated and selected data will be used to jointly fit these models (Extended Data Fig. 4 and ‘Bayesian data analysis and calibration’ and ‘Time- and antenna-dependent modelling’ sections in the Methods). The output of this Bayesian fitting process will result in constraints on fundamental cosmological parameters as well as foreground parameters. This will allow us to interpret the models and produce the desired scientific results (see the ‘Science prospects’ section for more details).

Going forward, we expect to add further functionality to both the system (for example, scaled antennas) and the analysis and calibration pipelines (for example, statistical analysis of the receiver residuals during the joint data analysis step). We furthermore envisage the validation of any result using a comprehensive end-to-end simulation.

Science prospects

The primary science goal of REACH is noise-limited detection and observation of the evolution with redshift of the sky-averaged 21-cm hyperfine line emission from the neutral hydrogen that pervaded the intergalactic medium (IGM) during the cosmic dawn and the epoch of reionization. The extreme challenge posed by strong foreground emission necessitates exquisite instrument modelling and data calibration in global 21-cm experiments. Ultimately, unless one can place strong priors on the parameters of models for

plausible systematic effects in the data, the robustness with which constraints on astrophysics can be derived from the data is limited. A list of additional science outputs for the experiment is included in the ‘Additional science outputs’ section in the Methods.

EDGES verification. A 500 mK absorption trough at $z = 17$, consistent with the signal inferred by EDGES, is detectable with $\lesssim 1/6$ th of the observing time necessary for bright standard 21-cm signal models at the same redshift. As such, verifying the EDGES detection is the initial science goal of REACH. The EDGES analysis of their data utilizes a flattened Gaussian parameterization of the brightness temperature of the global 21-cm signal (T_b),

$$T_b(\nu) = -A_{\text{flatG}} \left(\frac{1 - e^{-\tau e^{B_{\text{flatG}}}}}{1 - e^{-\tau}} \right), \quad (1)$$

where

$$B_{\text{flatG}} = \frac{4(\nu - \nu_0)^2}{w^2} \log \left[-\frac{1}{\tau} \log \left(\frac{1 + e^{-\tau}}{2} \right) \right], \quad (2)$$

and A_{flatG} , ν_0 , w and τ describe the amplitude, central frequency, width and flattening of the absorption trough, respectively.

The presence in REACH data of a 21-cm signal that is consistent with that reported by EDGES can directly be constrained within the REACH analysis pipeline by performing a joint fit for the most probable model of the foregrounds and the global 21-cm signal model of the form shown in equation (1), with priors on A_{flatG} , ν_0 , w and τ given by their posteriors in the EDGES analysis. As little as ~ 3 h of integrated data out of approximately 30 h of observations, obtained over several nights (quietest ionosphere and lowest RFI) will enable us to verify the presence or absence of an EDGES signal of this form.

Beyond placing constraints on the presence of the global 21-cm signal inferred by EDGES directly, we will constrain the presence of a

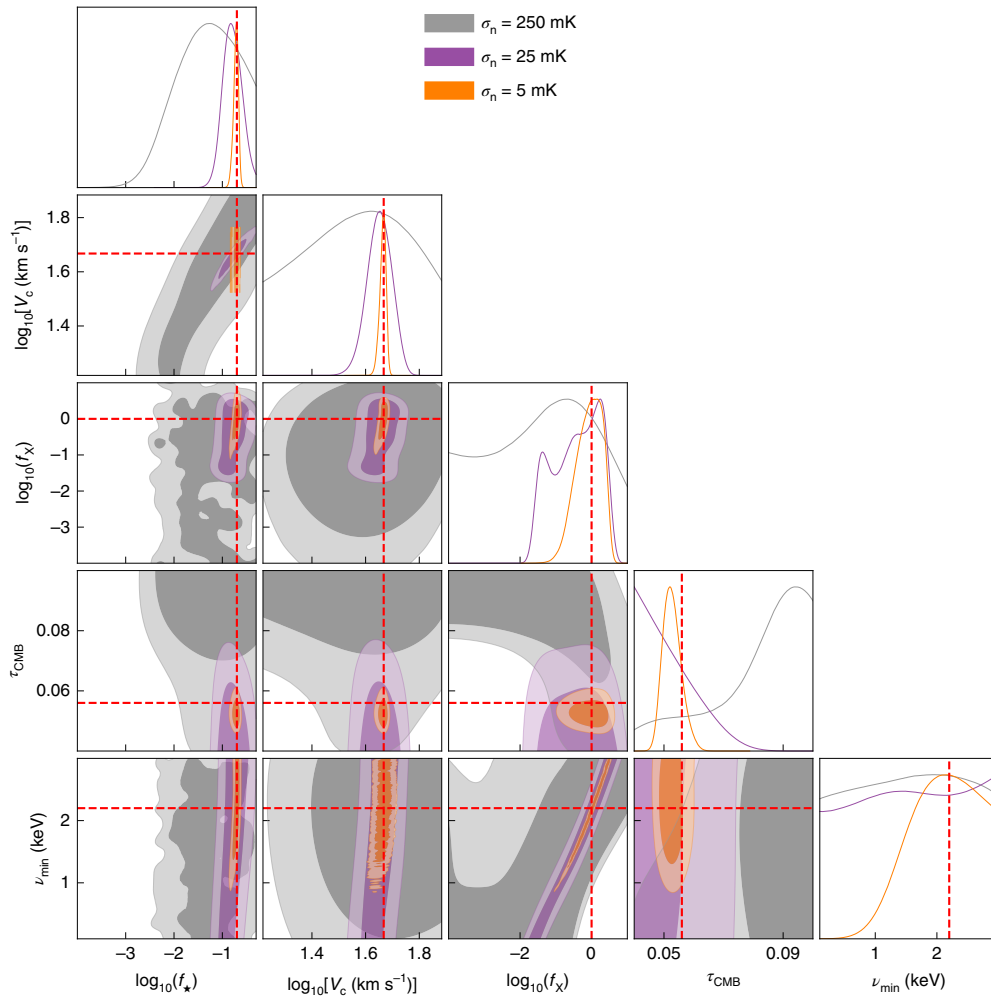


Fig. 5 | Posterior probability distribution forecasts of constraints on 5 astrophysical parameters characterizing the evolution of the 21-cm brightness temperature during cosmic dawn and the epoch of reionization. Forecasts are based on recovery of the astrophysical parameters of a fiducial 21-cm-signal model (with input parameters shown with red dashed lines) from REACH datasets at three noise levels (σ_n): 250 mK (grey), 25 mK (purple), 5 mK (orange). The darker shaded areas represent the 1 standard deviation regions of the posterior probabilities for all pairs of parameters and the lighter shaded areas represent the equivalent 2 standard deviations regions. In the diagonal we show the 1D posterior probabilities for all the individual parameters. The parameters being constrained are f_* , the star-formation efficiency; V_c , the minimum virial circular velocity of star-forming galaxies; f_X , the X-ray efficiency of sources; τ_{CMB} , the CMB Thomson-scattering optical depth; and ν_{min} , the low-energy cutoff frequency of the X-ray spectral energy distribution (α , the power-law index of the X-ray spectral energy distribution and R_{mfp} , the mean free path of ionizing photons in the IGM, are fixed in this analysis to 1.3 and 30.0 Mpc, respectively, since they tend to have a smaller influence on the global 21-cm signal).

high-amplitude global 21-cm signal more generally by fitting physically motivated exotic models for the 21-cm signal. If a 21-cm cosmic dawn absorption trough with an amplitude in excess of ~ 200 mK at $z=17$ exists in nature, it implies an increased differential brightness between the hydrogen spin temperature and the radio background relative to standard cosmological models. As described above, this requires that either the radio background temperature is larger than expected, which would occur if there were an unaccounted-for radio background in excess of the CMB^{9,10,17,18,50–53}, or that the hydrogen kinetic temperature and, correspondingly, the spin temperature (following Wouthuysen–Field coupling to the kinetic temperature) is cooled to below the level expected from adiabatic cooling alone^{54–58}.

If REACH measurements find a 21-cm signal consistent with that inferred by the EDGES team, or, more generally, one in excess of standard astrophysical models for cosmic dawn, we will fit 21-cm global signal simulations modelling each of these scenarios. In this case, we will place constraints on the presence of both standard astrophysical and exotic sources of excess radio background emission¹⁰, as well as dark matter cooling of the hydrogen gas⁹.

Constraining a standard amplitude 21-cm signal. If REACH measurements do not support the EDGES detection as we continue to integrate down, the absence of a high-amplitude signal will enable us to place stringent constraints on the amplitude of an excess radio background and on the physical mechanisms that can cool the hydrogen kinetic temperature to below the temperature expected from adiabatic expansion alone.

In this scenario, if continued integration leads to the detection of a standard astrophysical 21-cm signal, we will use 21-cm-signal forward modelling consistent with standard astrophysical and cosmological assumptions to constrain astrophysical and cosmological parameters given our data.

Figure 5 illustrates the level of constraints on the properties of the IGM and the first luminous sources that would be inferred from a detection of a fiducial global 21-cm signal in the REACH spectral band in the limit that instrumental noise is the only source of uncertainty on the signal in the data. In practice, correlation between the foreground and signal models will increase the uncertainties on recovered 21-cm signal parameters; thus, Fig. 5 represents a

best-case scenario for the precision to which astrophysical parameters can be constrained at the quoted noise levels. The constraints, so derived, are illustrated for three noise levels: 250 mK (grey), 25 mK (purple), 5 mK (orange). (For simplicity, Gaussian white noise has been added to the signal in the simulated dataset. However, a more realistic radiometric noise model is under development and will be employed for analysis of REACH data.) These correspond to the expected noise levels in datasets comprising observations centred on low-foreground regions of the sky, away from the Galactic plane, in a 100 kHz channel, at a reference frequency of 50 MHz and with total observation times of ~ 1 , 100 and 2,500 h, respectively. We treat these values as illustrative of pessimistic, fiducial and optimistic scenarios, respectively, for the non-systematics-limited noise levels that will be obtained with REACH. We define our fiducial scenario here with reference to the 25 mK root mean square (r.m.s.) of data-minus-sky-model residuals in EDGES low-band data found in ref. ¹⁷.

In practice, the specific constraining power of a REACH dataset will depend on the shape and depth of the 21-cm signal relative to the noise in the data. Nevertheless, Fig. 5 is illustrative of the general properties of the IGM and the first luminous sources that can be well constrained by data in the REACH band, with precision constraints on f_{\star} , V_{\odot} , f_X , τ_{CMB} and ν_{min} obtained in the high signal-to-noise regime.

The 21-cm-signal model in Fig. 5 uses the globalemu global signal emulator⁴² of simulations by refs. ^{9,10,20,59,60}; however, alternate global signal modelling tools such as ARES (Accelerated Reionization Era Simulations)⁶¹ are also available for use to the same end (see the ‘Cosmological models’ section in the Methods for more details).

Conclusion

The REACH experiment has been conceived to provide a confident detection and subsequent analysis of the sky-averaged 21-cm signal from primordial hydrogen, a signal emitted at the time of the birth of the first stars and the epoch of reionization. Featuring a suite of Bayesian analysis and calibration techniques, the experiment improves over current efforts and their sensitivity to hardware systematics by exploiting a joint analysis of the cosmological signal, the contaminating foregrounds and the instrument itself. This joint analysis provides us with several advantages, including access to the Bayesian evidence for the data and models as well as better understanding of the correlations between the different signal components. Two wideband radio antennas will simultaneously observe the Southern Hemisphere sky from the base at the Karoo radio reserve in South Africa. As shown in the manuscript, the use of simultaneous observations with two different antennae helps us enhance the precision of the detection as well as remain more insensitive to specific hardware-related systematics. With a wide redshift coverage of 7.5–28, REACH will also use a novel in-field calibration technique using Bayesian parameter estimation of calibration coefficients. This approach allows us to further isolate systematic and hardware-related features from spectral features belonging to the sky signal. In this Article, we reported the experiment aims, system design, data pipelines and science predictions, highlighting the ability of the experimental approach to produce confident constraints on cosmological models.

Methods

Exotic interpretations of the EDGES signal. To explain the depth of the feature reported by the EDGES collaboration, several exotic theoretical interpretations have been argued by the community. A solution can be obtained by achieving a stronger contrast between the spin temperature of the 21-cm transition and the temperature of the radio background radiation at the intrinsic wavelength of 21 cm. Several physically motivated scenarios have been described in the literature, of which the most popular include overcooling of the hydrogen gas beyond the adiabatic cooling limit via interactions with cold dark matter^{34–58} or producing extra high-redshift radio background contribution in addition to the

omnipresent CMB^{9,10,17,18,50,51,53,62,63}. In the former case, the overcooling is mediated by millicharged cold dark matter particles interacting with ordinary matter and draining excess energy from the gas. Taking into account existing astrophysical, cosmological and particle physics constraints, recent studies indicate that the mass of a millicharged cold dark matter particle should be between 10 MeV and a few hundreds of GeVs with a dark matter energy density fraction between 10^{-8} and 0.004 to explain EDGES³⁸. In the alternative scenario of an excess radio background, anomalously bright high-redshift astrophysical sources, a thousand times stronger than the familiar radio-loud active galactic nuclei^{51,53,64–66} or star-forming galaxies^{10,67,68}, are required to sufficiently raise the radio background and explain the EDGES detection. Alternatively, extra radio background could be produced by exotic processes such as radiative decay of particles, annihilating dark matter or super-conducting cosmic strings^{52,69–73}. Other potential explanations include dark matter spin-flip interactions with electrons through a light axial-vector mediator directly inducing a 21-cm signal⁷⁴.

EDGES data re-analysis. The spatial spectral structure of the sky radiation, when convolved with the spatial spectral antenna beam, produces spectral structure not easily modelled by a low-order polynomial. A simulated analysis of this effect is provided in Supplementary Fig. 5.

It has been hypothesized^{27–30} that this kind of hardware-residual systematic signals could be, at least in part, the explanation for the anomalous absorption profile published by the EDGES team¹⁷. The EDGES team described in detail in that publication their process to calibrate the foreground signal and hardware systematics, and they presented a comprehensive set of validation observations to support their choice of models and calibration. In that work, a physically motivated polynomial-based model is used to calibrate the foreground signal after the beam chromaticity has been corrected for. However, while physically motivated, this foreground modelling used non-physical parameters and could be susceptible to model hardware systematics and potentially the cosmological signal itself, as shown in ref. ²⁷.

In the top-left of Extended Data Fig. 1 we demonstrate that if the foreground models are restricted to physical parameters²⁷ (purple) versus unrestricted foregrounds (orange), the detected signal from the EDGES public data could look quite different. Furthermore, the bottom-left of Extended Data Fig. 1 shows the best fit for the EDGES public data by using standard astrophysical models of the cosmological signal²¹ instead of a flat Gaussian model as is used in ref. ¹⁷. The right column of Extended Data Fig. 1 shows the residuals after subtracting the posterior average foreground and signal models from the EDGES public data in each case. The r.m.s. values of the residuals are 0.023 K for the case of unrestricted foregrounds and a flattened Gaussian signal, 0.122 K for the case of restricted foregrounds and a flattened Gaussian signal, 0.077 K for the case of unrestricted foreground and a 21cmGEM (21-cm Global EMulator) signal and 0.215 K for the case of restricted foregrounds and a 21cmGEM signal. It is worth noting, however, that in ref. ¹⁷ a series of tests are presented showing the insensitivity of the result to field hardware modifications.

Antennas. In REACH Phase I observations will be performed with two different antennas, in overlapping frequency bands, to detect and isolate antenna hardware systematics. These antennas will be installed on top of a 20×20 m metallic ground plane with serrated edges to minimize edge reflections. A multi-level design approach is followed in the development of the antennas. At the top level, the general topology is down-selected, and more detailed designs are performed at lower levels of the most promising set of antenna types.

The first level of down-selection is informed by a set of figures of merit describing the chromaticity of the antenna beam, as well as the impedance frequency response. A smooth beam is enforced by minimizing the variance of the chromaticity factor $C(t, \nu)$. The original goal of this factor^{75,76} is to correct for the spectral structure introduced by the beam with respect to a given reference frequency within the band. It is defined as

$$C(t, \nu) = \frac{\int_{\Omega} T_{\text{sky}}(t, \nu_{\text{ref}}, \Omega) D(\nu, \Omega) d\Omega}{\int_{\Omega} T_{\text{sky}}(t, \nu_{\text{ref}}, \Omega) D(\nu_{\text{ref}}, \Omega) d\Omega}, \quad (3)$$

where

$$T_{\text{sky}}(t, \nu_{\text{ref}}, \Omega) = [T_{\text{base}}(t, \Omega) - T_{\text{CMB}}] \left(\frac{\nu_{\text{ref}}}{\nu_{\text{base}}} \right)^{-\beta} + T_{\text{CMB}} \quad (4)$$

and $D(\nu, \Omega)$ is the antenna directivity, ν_{ref} is the reference frequency, Ω is the direction on the sky, $T_{\text{base}}(t, \Omega)$ is an all-sky base map at frequency ν_{base} , t is the time of observation and T_{CMB} is the CMB temperature. For the impedance response, we sought to maximize the frequency bandwidth where reflections into a 50 Ω load are below -10 dB in magnitude, while enforcing that the lowest reflection levels occur in the 50–170 MHz band. Additionally, we prefer antennas with smoother impedance variation over frequency, as these are generally easier to model in computational electromagnetics solvers.

The point of simple modelling is also considered in the down-selection process. Smaller antennas, with mechanically simpler structures, are generally

easier to manufacture and model accurately. We expect better correlation between simulations and measured results for simple antennas than for more complex structures, and thus more accurate feature extraction due to small geometric and material variations.

Once a few promising candidate antennas have been identified by the process above, a more complete pipeline analysis (briefly described in the ‘Data-analysis-driven antenna selection’) is performed on the nominal structures to estimate the likelihood and goodness of a simulated signal detection process. Since these analyses are extremely time consuming, they are not used in the direct optimization loop. Results from the pipeline simulations identified the conical log-spiral and horizontal hexagonal dipole antennas (Fig. 2) as the most promising structures. While the spiral antenna has a broader operating bandwidth than the dipole, it is mechanically more complex. The substantial difference in radiating mechanisms between these antennas, however, make them an attractive pair for REACH where we will use both antennas to identify and isolate hardware systematics in the analysis pipeline. We also note that the hexagonal dipole antenna shown in this manuscript is similar in type to the square dipole antenna used by the EDGES experiment.

The final antenna geometry is fine-tuned in a detailed optimization loop, where a parametric model of the main response features (both beam and impedance) is simultaneously extracted as a function of small variations in geometry around the nominal values. Details of this process are reported in ref. 40.

Data-analysis-driven antenna selection. The different antennas under consideration were analysed using a simulated version of the Bayesian data analysis pipeline, which is described in the ‘Foreground models and chromaticity correction’ section, as one of a number of figures of merit used to decide upon antenna designs (Fig. 4). This assessment was based on our ability to reconstruct a range of injected mock 21-cm signal in simulated data with both a high degree of statistical confidence and a small r.m.s. error with respect to the injected signal for different simulated antenna patterns.

The REACH data analysis pipeline is designed to correct for systematic distortions of data due to chromaticity of the antenna. However, certain structures of chromatic distortion can be more difficult to correct for than others. Therefore, testing how well a range of signals are recovered from simulated data (which includes modelling of the distortions from the antenna) using the pipeline as part of the design process helps identify what antenna designs are more suited to the experiment. This process is described in detail in ref. 39. A summary of this selection strategy is provided in Supplementary Fig. 6.

Receiver and calibrator. The REACH radiometer uses the noise waves formalism⁷⁷ to determine critical calibration coefficients. Its primary aim is to achieve milli-Kelvin level calibration of the sky signal by correcting for the antenna mismatch and receiver response including the analogue-to-digital converter. This is achieved by careful design of the RF components in the chain and the use of very-high-quality calibration sources at known temperatures.

The REACH radiometer presents the ultimate in instrumental calibration capability because it relies purely on field-gathered data that are fully autonomous, requiring no physical interaction once installed, meaning that calibration and observation can happen concurrently. The details of the noise waves, along with the Bayesian receiver calibration pipeline we have developed that employs conjugate priors to compute coefficients quickly in the field, can be seen in the ‘Bayesian receiver calibration’ section. A full description can be found in ref. 38. Furthermore, the radiometer shown in Fig. 2 can easily incorporate many ‘calibration sources’ and is currently envisaged to have 13 independent calibrators all feeding data into the receiver calibration pipeline.

The calibration system employs mechanical switches that have very low loss (typically 0.01 dB in this band) and better than 100 dB isolation. A transfer switch allows a VNA to measure the reflection coefficients of the sources and the low-noise amplifier (LNA). An on-board micro-controller facilitates this process along with controlling the environmental temperature. All signals (control and RF) are transported via RF-over-fibre cables to avoid interference and extra loss to a readout system that converts signals back into RF and digitizes them. The calibration sources used offer strategic sampling of the noise waves as a function of impedance and go much further than a standard open or shorted cable. More information on this is provided in Supplementary Fig. 1.

In a normal observation, REACH will rely on Dicke switching to observe the sky, an ambient load and a noise source on regular intervals of 10–30 seconds. Using these three power spectral densities measured with the spectrometer we can calibrate out the effects of the receiver system.

The first major component in the RF chain is the LNA that is in the field unit under the antenna. It is designed to have a very flat spectral response both in terms of scattering parameters (S-parameters) and noise. This component is followed by a RF-optical transducer (AMP1), which converts the signal into an optical signal. The optical signal from the field unit is converted back into RF with AMP2 in the back-end, where out-of-band noise (DC–25 MHz) is also injected for conditioning of the spectrometer. Finally, the signal is split and fed to both a high-resolution power meter and the spectrometer, running side by side. This offers additional information that can be used in the calibration process. The passband response of

the REACH receiver system along with the measured LNA response is provided in Supplementary Fig. 2.

Bayesian receiver calibration. REACH uses a novel calibration algorithm developed from the formalism introduced in the EDGES experiment¹⁷. The calibration strategy follows the method established by Dicke⁷⁸ to characterize systematic features of radio-frequency instruments through measurements of multiple calibration standards to determine ‘noise wave parameters’; the portion of noise reflected by the antenna that is uncorrelated with the output noise of the LNA (T_{unc}), the portions of reflected noise correlated with noise from the LNA (T_{cos} and T_{sin}), and T_{NS} and T_{L} , which are assumptions for the noise temperature of the excess noise temperature of the internal noise source above ambient and the internal reference load, respectively (refs. 77,78). These noise wave parameters describe reflections arising at connections within the experimental apparatus that re-enter the receiver along with the measurement. The use of noise wave parameters allows for the derivation of a relationship between the calibrated temperature of any source, T_{source} , and power spectral densities measured by the receiver³⁸

$$T_{\text{NS}} \left(\frac{P_{\text{source}} - P_{\text{L}}}{P_{\text{NS}} - P_{\text{L}}} \right) + T_{\text{L}} = T_{\text{source}} \left[\frac{1 - |F_{\text{source}}|^2}{|1 - F_{\text{source}} F_{\text{rec}}|^2} \right] + T_{\text{unc}} \left[\frac{|F_{\text{source}}|^2}{|1 - F_{\text{source}} F_{\text{rec}}|^2} \right] + T_{\text{cos}} \left[\frac{\text{Re} \left(\frac{F_{\text{source}} F_{\text{rec}}}{1 - F_{\text{source}} F_{\text{rec}}} \right)}{\sqrt{1 - |F_{\text{rec}}|^2}} \right] + T_{\text{sin}} \left[\frac{\text{Im} \left(\frac{F_{\text{source}} F_{\text{rec}}}{1 - F_{\text{source}} F_{\text{rec}}} \right)}{\sqrt{1 - |F_{\text{rec}}|^2}} \right], \quad (5)$$

where P_{source} , P_{L} and P_{NS} are measured power spectral densities of the receiver input, internal reference load and internal reference noise source, respectively. F represents measured reflection coefficients of the same source (F_{source}) and receiver (F_{rec}). We may condense our calibration equation into a linear relationship for simplicity

$$T_{\text{source}} = X_{\text{unc}} T_{\text{unc}} + X_{\text{cos}} T_{\text{cos}} + X_{\text{sin}} T_{\text{sin}} + X_{\text{NS}} T_{\text{NS}} + X_{\text{L}} T_{\text{L}}, \quad (6)$$

where X_{unc} , X_{cos} , X_{sin} , X_{NS} and X_{L} are initial calibration measurements as defined in ref. 38. Taking advantage of the linear form of our equation, we may group our terms into a matrix containing our data, X , and a matrix of calibration parameters, Θ

$$X \equiv (X_{\text{unc}} \quad X_{\text{cos}} \quad X_{\text{sin}} \quad X_{\text{NS}} \quad X_{\text{L}}) \\ \Theta \equiv (T_{\text{unc}} \quad T_{\text{cos}} \quad T_{\text{sin}} \quad T_{\text{NS}} \quad T_{\text{L}})^{\top}. \quad (7)$$

Our calibration equation, where \top is the matrix transpose operator, can now be solved using a linear regression model

$$T_{\text{source}} = X\Theta + \sigma, \quad (8)$$

with our noise term, σ . This allows for a joint solution of all terms, instead of an iterative approach as used in previous experiments such as EDGES⁷⁹.

The application of conjugate priors within our Bayesian methodology enables our algorithm to be many orders of magnitude faster than techniques that use full numerical sampling via Markov chain Monte Carlo methods over many parameters. This allows for an in-place calibration with the data acquisition instead of relying on off-site measurements. Individual noise wave parameters are optimized using a gradient-descent algorithm rather than applying a blanket fit multi-order polynomial to all noise wave parameters. Correlation between noise wave parameters is also considered in the derivation of their values, as shown in Extended Data Fig. 2 (ref. 38). A schematic of the calibration algorithm is shown in Extended Data Fig. 2. Preliminary trials using this technique, applied to eight calibration standards, successfully derive the temperature of a 50 Ω load resulting in an r.m.s. error of 8 mK between calibrated and measured temperatures, well within a 1 σ noise level and comparable with the calibration accuracy of the EDGES experiment^{38,79}.

Digital back-end. The digital back-end (or REACH spectrometer) is based on the FPGA digitizer and beamformer board developed for the SKA1 Low Frequency Array⁸⁰. This board, known as TPM, hosts 16 high-performance Analog Devices AD9680 14 bit dual-channel analogue-to-digital converters (ADCs) and two Xilinx Ultrascale FPGAs. The board has been successfully used in the context of the Aperture Array Verification System for SKA⁸¹ and in several other instruments^{82–84}. Together with its firmware and software libraries⁸⁵, the TPM provides a platform for fast development of radio-astronomy digital back-ends. In this context, the auxiliary functions, such as communication over gigabit ethernet for monitoring and control and data acquisition, are reused with minimal modifications, while the FPGA firmware is customized to support the specific application requirements. Specifically, a high-performance digital spectrometer was developed, where each FPGA processes a single digitized RF signal. Each TPM can thus process two RF signals, with the unused ADCs being powered down to save power. This

arrangement allows for the implementation of a full floating-point digital signal processing pipeline that includes a polyphase filterbank and power integrator. The key parameters of the TPM spectrometer are summarized in Supplementary Table 1.

We note that an important aspect of the digital back-end is the channel isolation, which we have measured to be 90 dB (side-lobe rejection at the adjacent channel centre) as shown in Supplementary Figs. 3 and 4. This value is especially relevant in the context of RFI excision. While deeper RFI measurements are needed, our initial measurements⁸⁶ and experience with co-located experiments (for example, HERA) indicate that this value could be good enough already.

The polyphase filterbank uses a weighted overlap-add architecture supporting a total number of 229,376 tap coefficients, which can be downloaded to the FPGA, allowing for the use of different weighting functions without re-compiling the FPGA firmware. Power spectra are accumulated over a programmable number of fast Fourier transform frames that is set to a corresponding integration time of about ~1 s. Accumulated spectra are then transmitted to the processing server where they can be accumulated further. The back-end control software is responsible for the correct, timely and safe operation of all the controllable hardware making up the on-site deployed system. It is responsible for configuring, initializing and controlling the required components for the correct running of observations defined by the operator. An observation includes a number of steps, with receiver calibration, continuous source switching, spectra accumulation and hardware monitoring being some of the primary ones. Upon observation completion, the generated output files can then be transferred off-site through the satellite network link.

Site and RFI. Conventional approaches to the analysis of 21-cm data fundamentally assume that spectrally smooth astrophysical foregrounds can be discriminated from the predicted spectral structure of the 21-cm signal. Highly chromatic, terrestrial RFI is several orders of magnitude brighter than the spectral foregrounds, whose brightness itself already poses important challenges to the 21-cm analysis pipeline. The spectral structure of RFI, if not carefully removed, could be considered as part of the spectral structure of the 21-cm signal itself. In an effort to mitigate the effects of RFI, the REACH instrument will be deployed at a radio-quiet site in the Karoo Radio Astronomy Reserve (‘the Reserve’) near the town of Carnarvon in the Great Karoo semi-desert in South Africa. The Reserve is shared with several other radio telescopes including the SKA mid-frequency core⁸⁴, MeerKAT⁸⁵, HERA⁸⁶, and HIRAX (Hydrogen Intensity and Real-Time Analysis eXperiment)⁸⁷, and offers critical support infrastructure to our experiment not always available at radio-quiet sites, such as well-maintained roads, on-site maintenance and engineering staff, and controlled access and entry. The site is located within seven hours drive of Cape Town, making it feasible for the Collaboration to routinely commission the instrument and also offer access to academic and manufacturing resource hubs.

Since most of the other instruments at the Reserve (especially the flagship SKA-Mid telescope) operate at higher frequencies, less severe restrictions are in place for radio transmissions at REACH operating frequencies in the surrounding region. As such, care was taken to select a site with minimal RFI at the REACH operating frequencies. The most problematic sources of RFI are FM radio transmitters serving surrounding communities, which operate in the band 88–108 MHz. After two extensive RFI measurement surveys, where a number of potential sites (informed by Longley–Rice propagation models with 1 km² resolution of the FM signals over the terrain of the Reserve, shown in Fig. 2) were investigated, the final site was selected on the basis of a combination of low RFI, access to a nearby road and favourable topography. Details of the measured RFI results for several sites, as well as a full description of the methodology and measurement calibration, are provided in ref. ⁸⁶. The site (30°50′16.75″ S; 21°22′27.22″ E), depicted in Fig. 2, is a large flat plane of approximately 4 km in diameter, surrounded on all sides by mesas and hills. Although the interference from FM radio transmitters is reduced at this site, it is still present at a low level and several narrow bands must be masked out in the final data analysis pipeline. The interfering power levels are low enough to be of no concern for saturating the receiver.

High-level system metrics. The REACH Phase I instrument features two radiometer systems. The first one uses a wideband hexagonal dipole antenna covering a frequency band of 50–130 MHz, with zenith directivity of 7.0 dBi and a radiation efficiency of 0.9. The receiver noise temperature equals 600 K for this radiometer. The second radiometer system uses a conical log-spiral antenna covering a frequency band of 50–170 MHz, with zenith directivity of 11.0 dBi and a radiation efficiency of 0.98. The receiver noise temperature equals 600 K for this radiometer as well.

With these parameters, the minimum required integration time to detect an EDGES-like signal (0.5 K) with a signal-to-noise ratio of 10:1 on 100 kHz coarse channels would be ~6.5 h with the dipole system and 7.3 h with the conical log-spiral system. A standard 0.15 K signal centred at 100 MHz would require ~29 h with the dipole system and 31 h with the conical log-spiral. Meanwhile, an exotic deep signal (0.5 K) centred at 130 MHz would require only ~1.3 h with the dipole and a very similar number with the conical log-spiral. These simplistic

estimates are purely based on a radiometer equation calculation and meant to give a first-order estimate of the required integration time for the REACH system depicted in this manuscript. In reality, observations will need to last at least an order of magnitude longer since, for example, we will need to flag and blank a large amount of low-quality data (for example, contaminated by RFI) and to spend part of the observation time calibrating the receiver unit.

Instrument models. A fundamental component of the data analysis pipeline is the use of parametrized physically motivated instrument models accounting for the response of the radio telescope to the sky signal across angular space, time and frequency. Especially important is the ability to account for environmental effects and interaction with the environment (for example, the soil underneath the antenna). Within REACH, we are developing these models using a suite of tools that includes: full wave electromagnetic simulations, neural network emulators, lab measurements of components, measurements of scaled prototypes in control environments (for example, radio anechoic chambers), in-field measurements using unmanned aerial vehicle platforms⁸⁸ and so on.

The impact of soil and ground plane truncation on the electromagnetic properties of the antenna will be taken into account using the method described in ref. ⁸⁹. Using this method, the S-parameters and radiation patterns of the antenna do not suffer from a lack of accuracy resulting from the use of the method of images. In ref. ⁸⁹, a full wave solver is developed to solve the Maxwell’s equations in their integral form. This method is based on a spectral formulation of the method of moments, which uses inhomogeneous plane waves to describe the interactions between the antenna and the finite ground plane. In a nutshell, the antenna equivalent currents are decomposed into a spectrum of inhomogeneous plane waves that is integrated to obtain the spatial electric field radiated by the antennas on the ground plane. This field is then integrated on the ground plane equivalent currents and the method of moments linear system of equations is solved. The field incident to the ground plane can be expressed as follows:

$$\mathbf{E}_p(x, y, z) = \frac{-jk\eta}{(2\pi)^2} \int \int F_p(k_x, k_y) \times \frac{e^{-j(k_x x + k_y y - k_z z)}}{2jk_z} \left[\hat{\mathbf{e}}_p^d + \Gamma_p(\beta) \hat{\mathbf{e}}^u \right] dk_x dk_y, \quad (9)$$

where $F_p(k_x, k_y)$ is the antenna radiation pattern, (k_x, k_y, k_z) are the components of the wave vector, j is the imaginary number, k is the wavenumber, η is the medium impedance, $\hat{\mathbf{e}}$ is the polarization vector, $\hat{\mathbf{e}}_p$ is the polarization vector of polarization p (either transverse electric or transverse magnetic) and $\Gamma_p(\beta)$ is the reflection coefficient due to the presence of the soil. This is an efficient formulation to compute the interactions between an antenna and a ground plane with electrically small diameter ($< \lambda_0$, with λ_0 the free space wavelength). In ref. ⁸⁹, an accelerated formulation based on analytical Hankel transforms is derived to efficiently handle the interactions with large ground planes. This second formulation is efficient to compute the intermediate electric field (distances greater than λ_0). Combined with the inhomogeneous plane waves method, the electric field can be rapidly evaluated everywhere on the ground plane. Finally, these models will be informed with measurements of the soil layers using a ground penetration radar system.

Bayesian data analysis and calibration. Theoretically, the temperature of the sky $T_{\text{sky}} = T(\Omega, \nu, t)$ is a function of angle Ω , frequency ν and time t . We work in earth coordinates, with the sky rotating over us providing some of the time variation, and the other portion arising from time-dependent foregrounds such as the ionosphere. We therefore decompose the raw sky signal into the global signal $T_g(\nu)$, which is constant across the sky and time, the foregrounds T_f and statistically random components N_{sky}

$$T_{\text{sky}}(\Omega, \nu, t) = T_g(\nu) + T_f(\Omega, \nu, t) + N_{\text{sky}}(\Omega, \nu, t). \quad (10)$$

This equation makes explicit the standard modelling split between elements of the system that we can model deterministically (T_g and T_f) and elements that, at best, we can model probabilistically (N_{sky}). In practice, a global experiment collects data, T_{obs} , from the full sky convolved with an antenna directivity D :

$$T_{\text{obs}}(\nu, t) = \int T_{\text{sky}}(\Omega, \nu, t) D(\Omega, \nu) d\Omega + N_{T_{\text{obs}}}(\nu, t). \quad (11)$$

This process introduces its own random noise, $N_{T_{\text{obs}}}$, associated with the calibrator⁸⁸. In this notation, we take a broad definition of beam modelling D that, for example, in addition to taking hardware into account can also include the effects of the ionosphere through an augmented angle argument Ω (ref. ⁴¹). Assembling these pieces, we have:

$$T_{\text{obs}}(\nu, t) - T_g(\nu) - \int T_f(\Omega, \nu, t) D(\Omega, \nu) d\Omega = N(\nu, t), \quad (12)$$

$$N(\nu, t) \equiv N_{T_{\text{obs}}}(\nu, t) + \int D(\Omega, \nu) N_{\text{sky}}(\Omega, \nu, t) d\Omega \quad (13)$$

where the random portions have been combined into a single random noise variable N . A common next step is to then ‘integrate’ this over time, but this is

only strictly necessary if data compression is required for storage purposes. In practice, most likelihoods will perform an effective integration step and to speed up computation one can usually do this sum early on, but it is important to conceptually separate convenience from necessity for now.

The statistical approach is to then use the random distribution of N to generate a likelihood. For simplicity and concreteness, if we assume that N is Gaussian and uncorrelated in time and frequency with noise level σ , the probability of observing the antenna data, T_{obs} , is

$$P(T_{\text{obs}}|T_g, T_f, D) = \prod_{\nu, t} \frac{1}{\sqrt{2\pi}\sigma} e^{-N^2/2\sigma^2} \Rightarrow \log P(T_{\text{obs}}|T_g, T_f, D) \\ = -\sum_{\nu, t} \log(\sqrt{2\pi}\sigma) + \frac{1}{2\sigma^2} (T_{\text{obs}} - T_g - \int T_f D d\Omega)^2. \quad (14)$$

This approach can, of course, be extended to a more sophisticated noise model (for example, to a σ model with varying frequency ν or correlations, or using an explicit calibrator derived setup). It is also worth noting that from a statistical perspective, this is what is being implicitly assumed whenever one performs a least-squares fit between model and data. For our REACH setup, after calibration the noise model is in fact a Student's t distribution, rather than a Gaussian, and our final pipeline will use Bayesian model comparison for the final likelihood design and selection⁴³.

The quantity in equation (14) is termed the likelihood $P(T_{\text{obs}}|T_g, T_f, D)$, and is the cornerstone of both frequentist and Bayesian approaches. Both approaches then often begin by parameterizing the unknown components: the global signal $T_g = T_g(\nu; \theta_g)$, the foregrounds $T_f = T_f(\nu, \Omega, t; \theta_f)$, and the directivity $D = D(\Omega, \nu; \theta_D)$, where θ_g , θ_f and θ_D are each vectors of parameters, and we denote all parameters as $\theta = (\theta_g, \theta_f, \theta_D)$. The likelihood can then be viewed as a function of these parameters:

$$P(T_{\text{obs}}|\theta) \equiv P(T_{\text{obs}}(\nu, t)|T_g(\nu; \theta_g), T_f(\nu, \Omega, t; \theta_f), D(\Omega, \nu; \theta_D)). \quad (15)$$

These parameterizations may be physical, phenomenological or non-parametric. For example, in the case of the global signal, we may wish to use signals generated by an emulator (for example, 21cmGEM²¹ or globalemu⁴²) parameterized by physical parameters of the early universe, or a phenomenological flattened Gaussian or a non-parametric free-form fit to the dip using a spline or polynomial approach⁹⁰.

The Bayesian approach treats the parameters θ as unknown variables. After stating a prior $P(\theta)$, we proceed to compute the likelihood and evidence via Bayes theorem:

$$P(\text{Data}|\theta)P(\theta) = P(\theta|\text{Data})P(\text{Data}). \quad (16)$$

$$\text{Likelihood} \times \text{Prior} = \text{Posterior} \times \text{Evidence}. \quad (17)$$

Laid out in this non-conventional form⁹¹, Bayes theorem states that our inputs to inference are a likelihood $P(\text{Data}|\theta)$ and prior $P(\theta)$, and our outputs are a posterior $P(\theta|\text{Data})$ and evidence $P(\text{Data})$. The posterior tells us our degree of knowledge of the parameters in light of the data, and can be used to marginalize out quantities that we are not interested in (nuisance parameters, such as the calibration or directivity details), and can also be used to produce forward inferences on quantities derived from these parameters, such as the global signal itself or the foregrounds. The evidence allows us to perform Bayesian model comparison to determine the quantitative merits of a given set of parametric models. This is critical on two fronts. First, it allows us to choose the best set of modelling assumptions and second, it allows us to determine the probability that there is a signal in the data in comparison with a fit where no global signal is included. Crucially, evidence does this in a way that generates Occam's Razor as a theorem⁹².

Nested sampling⁹¹ is a robust tool to numerically sample the full posterior and calculate the Bayesian evidence. Nested sampling is well suited for navigating a-priori unknown complex posterior surfaces that may or may not have multiple posterior modes and non-trivial covariance structure between parameters. Such structures regularly occur when fitting sophisticated non-parametric models where there are potential hidden degeneracies between signal and foreground⁹⁰. Our nested sampling implementation of choice is Polychord^{32,33}, whose slice-sampling-based approach represents the state of the art in nested sampling in high-dimensional parameter spaces and has the unique capability of being able to exploit a fast-slow parameter hierarchy, which occurs naturally in the context of 21-cm modelling.

Foreground models and chromaticity correction. Detailed data analysis processes are required in global 21-cm experiments such as REACH to separate the 21-cm signal from foreground emissions in the observing band. These foreground emissions come from many different sources, primarily Galactic synchrotron and free-free emissions, as well as extragalactic point sources⁹³. At the redshifts relevant to the global 21-cm signal, they can exceed the signal by up to four orders of magnitude. The first step in identifying the signal beneath these foregrounds is to exploit the fact that they are predominantly very spectrally smooth power-law emissions, whereas the signal is not^{94–96}. This would allow the signal to be identified by subtracting off smooth structure.

However, this process is made substantially more difficult by the presence of antenna chromaticity. The necessity of observing a wide frequency band makes the chromaticity in the pattern of the antenna very difficult to avoid. These changes in the antenna pattern with frequency then act to couple spatial variations in power on the sky into the frequency domain, resulting in non-smooth structure in the foregrounds that inhibits identification of the signal^{14,97–103}. If these distortions are not accurately corrected for, it can result in residual systematics in the data that can prevent detection of the signal^{27,29,30}.

One way of performing this correction is divide the data by a correction factor $C(t, \nu)$, defined in equation (3), as described in refs. ^{75,76,101}. Implementations of this correction, however, make assumptions such as that the sky at the frequency of the base map has the same spatial power distribution as at the reference frequency, that the spectral index of the foregrounds is uniform^{75,76} or that the simulated antenna pattern is an accurate model of the true pattern. These assumptions cannot be guaranteed in practice, which may result in this process leaving uncorrected-for systematics.

More sophisticated techniques for the correction of chromaticity distortion have also been proposed, for example, including a frequency-dependent sky brightness distribution¹⁰¹. Another proposed method exploits the possibility to model systematic effects using a single value decomposition analysis of simulated observations, possibly avoiding the need of accurate instrument models^{104–106}.

However, in keeping with the philosophy of the REACH project, we perform this correction, and the subsequent removal of foregrounds, by means of a new Bayesian data analysis pipeline that incorporates detailed physical modelling of the effect of chromaticity on the foregrounds⁹⁷. This allows an understanding of exactly what systematics are being removed.

In practice, this process works by generating parameterized approximate models of the full sky at all observing frequencies. The simplest way to do this would be to scale a known all-sky map by a single uniform spectral index parameter to the relevant frequencies. However, the spectral index actually varies across the sky^{46,75,76,107–110}, and if this is not accounted for, the resulting chromatic distortion models will not be accurate enough for the 21-cm signal to be identified. Therefore, we adopt a more detailed model that includes spectral index variation by subdividing the sky into N regions of similar spectral index, such as is shown in Extended Data Fig. 3 for $N=6$. A separate variable spectral index parameter can then be assigned to each region and a known all-sky map scaled by the resulting coarse-grained spectral index map to create the necessary parameterized sky model.

This sky model, $T_f(\Omega, \nu, \theta_\beta)$, parameterized by spectral index parameter θ_β , can then be convolved with the antenna beam model, $D(\Omega, \nu, \theta_A)$, parametrised by parameter set θ_A , as discussed above in a simulated observation, to produce a data model.

$$T_{\text{model}}(\nu) = \int_{\Omega} D(\Omega, \nu, \theta_A) T_f(\Omega, \nu, \theta_\beta) d\Omega. \quad (18)$$

The result of this is a foreground model that is parameterized by a physical property, the spectral index of the foreground emissions, and includes the chromatic distortions from the antenna as a part of the model. This allows the distortions to be fit from the data as part of the foreground rather than needing to be simulated and corrected for in advance.

We then propose to fit this foreground model to the data alongside a parameterized 21-cm signal model using the Bayesian nested sampling algorithm PolyChord^{32,33}. The foreground residuals and recovered 21-cm signals from fitting simulated data of log-spiral and hexagonal dipole antennas are shown in the rightmost column of Extended Data Fig. 3. Extended Data Fig. 3 also shows the results of fitting the simulated data with a log-polynomial model, with and without chromatic corrections of the chromaticity factor $C(t, \nu)$ (equation (3)), for comparison.

Using a nested sampling algorithm gives access to the Bayesian evidence. This can be used to allow the data to inform how many parameters are needed in the foreground and instrument models and thus prevent the data being fit with a foreground model of too many parameters, which might otherwise obscure the 21-cm signal. It also enables comparisons between models that include or do not include signal models, to quantify confidence in the presence of a signal, and comparisons between difference signal models.

By modelling the foregrounds and chromatic distortions together in a physically motivated manner, it enables the systematics that arise due to chromaticity to be well understood and accounted for. It also allows other sources of systematics, such as polarization¹¹¹ or ionospheric effects⁴¹, to be accounted for by expanding the physical model to include them. The simulations using the REACH pipeline in Extended Data Fig. 3 assume that the antenna beams are known exactly. As this is not possible in practice, we intend to develop this pipeline further to also fit for uncertainties in the beam model.

Time- and antenna-dependent modelling. The REACH data analysis pipeline is also designed to allow changes in the foregrounds and chromatic distortion due to changing observing time or from using different antennae to be exploited to model the foregrounds and 21-cm signal more accurately. Because the foreground

parameters being fit for by the pipeline are a physical property of the radio sky, the spectral index, the true values of these parameters should be unchanged for different times of observation and for observations with different antennae. The same is true for the 21-cm signal parameters.

As a result of this, it is possible with this pipeline to fit many datasets from different observing times and different antennae to corresponding models simultaneously in one likelihood, with them all informing the same parameter values. The effect of doing so, as opposed to fitting a single, time-integrated dataset to a single model, is shown in Extended Data Fig. 4.

Extended Data Fig. 4 (top-left) shows that, by fitting simulated data from both a log-spiral and a hexagonal dipole antenna simultaneously, the accuracy and precision of the recovered 21-cm signal are both improved. Signal accuracy is also seen to improve by fitting the data time bins jointly as separate datasets rather than integrating them. Furthermore, Extended Data Fig. 4 (top-right) shows that, for individual antennae, fitting data time bins separately results in an increase in the optimum number of foreground parameters needed, and so a more detailed model of the foregrounds in reconstructed relative to integrated data. However, when fitting data from both antenna simultaneously, both the time-separated and time-integrated versions require equally high detail in the foreground model.

As fitting data from multiple antennae simultaneously in particular can be seen from these results as producing improvement in both the detail of the foreground model and the accuracy of the recovered 21-cm signal, REACH is intending to deploy two antennae to be able to jointly fit data in this manner.

Detection of systematic errors. As detailed above, one of the driving principles when developing REACH has been the desire to account for and model systematics in the data analysis pipeline. For example, where experiments such as SARAS2²⁷ assumed an achromatic beam, REACH is using a data-driven development of the antenna and will account for chromaticity in the beam pattern directly with the foreground modelling.

However, regardless of how careful we are with our data analysis and calibration, the potential for unaccounted-for systematics not modelled in the Bayesian pipeline to enter the data remains. We have seen with existing experiments that systematics can cause uncertainty in the presence of global 21-cm signals^{27,29,30} and in some instances obscure any potential signal⁴⁸. Should the data from Phase I of REACH contain any unaccounted-for systematics, then a quick and accurate characterization of those systematics can lead to an identification of their cause and iterative improvements in the experimental system, calibration and/or data analysis.

Since the REACH Bayesian pipeline assumes the presence of specific known systematics, such as chromaticity in the beam and ionospheric effects, and then corrects for these alongside the foreground modelling, the presence of unaccounted-for systematics has the potential to distort these corrections and consequently the foreground model. This is true in particular of the chromaticity correction, which is driven by the raw data. This means that any residual systematics in the data after removing the modelled foreground and applying the distorted corrections may not be representative of the true unaccounted-for systematics. To accurately identify and characterize them, should they be shown to be present, we need, therefore, to separately model the foreground and known systematics such as chromaticity as accurately as possible. Particularly, the known systematics have to be modelled in a way that is either independent of the raw data or that includes comprehensive modelling of each component in the data, including the unaccounted-for systematic.

MSFs have been shown to be a useful foreground-modelling technique for global 21-cm experiments⁴⁵ and it has also been demonstrated that they can be used to accurately identify non-smooth systematics in datasets^{28,30}. They are functions that are constrained such that

$$\frac{d^m y}{dx^m} \geq 0 \text{ or } \frac{d^m y}{dx^m} \leq 0, \quad (19)$$

where m is the order of the derivative, meaning that they are characteristically smooth and can act as an effective model for the smooth synchrotron and free-free foregrounds in global 21-cm experiments. The constraint also prevents the functions from fitting out any non-smooth structure such as signals or systematics in the dataset, as can happen with an unconstrained polynomial. In the event that the Bayesian data analysis pipeline detailed above does not confidently identify a global 21-cm signal and illustrates the presence of systematics in the REACH data, we will use maxsmooth^{30,112} to fit MSFs to the calibrated data and help identify unaccounted-for systematics.

To do this, we will need to apply separate data-independent corrections for the expected chromaticity from the antenna beams and for other known systematics to the data. This will ensure that our MSF best represents the foreground and that any remaining residuals after modelling correspond to the unaccounted-for systematics.

We will attempt to physically model the structure left in the residuals after modelling known systematics and the smooth foreground. For example, any periodicity to the residuals could be linked to the reflections in cables or ground emission and the depth of discontinuities in the soil surrounding the antenna. By subsequently wrapping maxsmooth inside a Bayesian nested sampling loop with

and without various model components, including our physical model for the unaccounted-for systematic and various signal profiles, we can use the evidence of the different fits to determine whether the data favours the presence over the absence of our physical model or not. This can help provide confidence in our characterization of the unaccounted-for systematic or indicate that new physics are needed to describe the structure of the signals in the REACH data.

Assuming a correct characterization and functional description of any unaccounted-for systematics, we can confidently identify a cause that can then be mitigated in future iterations of the experiment. We can also use the functional description in unison with the Bayesian pipeline to fit for the unaccounted-for but subsequently characterized systematics, chromaticity correction, additional known systematics and foreground using nested sampling.

We provide a demonstration of the use of MSFs on EDGES low-band data in Supplementary Fig. 7.

Systematic signals in the data pipeline. Once a systematic error signal has been detected (for example, by running maxsmooth on the data) and identified, it is either corrected in hardware (for example, via hardware specific modifications/upgrades) or a model of the signal is included in the data analysis pipeline. Two possibilities exist in the latter case: either the model is parametric and the parameters can be jointly fitted together with the foreground and the cosmological signals, or the model is fixed.

Furthermore, to understand the ability of the data pipeline to cope with specific systematic signals expected in the REACH experiment, a series of simulated data analyses including such signals are performed. In Extended Data Fig. 4 (bottom-left), an example of such simulation is shown. In this simulation, a non-parametric (fixed) model of the antenna beam is used in which the presence of the finite metallic ground plane (20 × 20 m) below the antenna is used to both generate the data and for the model of the data pipeline. We note that this is not the ideal case, since ideally a parametric model of the beam capable of representing the effects of the ground plane is available and can be used. However, this simulation allows us to understand if the chromaticity introduced by a specific feature of the instrument design would result in the Bayesian analysis failing in the same way that certain antenna designs can do that. In Extended Data Fig. 4 (bottom-right), a simulated analysis where a specific systematic expected from the REACH design is both introduced in the data as well as modelled with a parametric model and fitted during the data analysis is shown. This simulation is for a systematic signal corresponding to uncalibrated reflections in the 6 m coaxial cable used to connect the conical log-spiral antenna to the receiver box. We note that for the dipole antenna this effect is a lot less worrying since the cable is much shorter (<0.5 m) and therefore any reflections produce data at scales of less concern for the detection of the global 21-cm signal. This simulation demonstrates that if an adequate parametric model is available, it is potentially possible to avoid the detrimental effect of a systematic signal and achieve a detection. Since the Bayesian evidence of these fits is available to us, it can be determined if the presence of the systematic signal is favoured or not. We note that currently we are developing parametric models for the antenna beam.

While these are scenarios where we have identified a potential systematic signal, the results help to demonstrate our ability to potentially make a detection even in the presence of such systematic signals. More information on this can be found in ref. 44.

Cosmological models. The 21-cm-signal simulations considered in this paper assume a standard astrophysical scenario (with the CMB as background radiation and astrophysical channels for cooling and heating of the gas).

The simulation methodology is semi-numerical and initially generates cosmological boxes of a few hundreds of comoving Mpc in which large-scale structure is evolved. The large size of the cosmological boxes is necessary to account for the nonlinear dependence of the global 21-cm signal on non-local astrophysical phenomena. Star formation is included at sub-grid level, as the simulations are aimed at large-scale 21-cm signals. The simulations are initialized with cubes of density, temperature and relative velocity between dark matter and baryons¹¹³. The density and velocity fields are evolved using linear perturbation theory. The number of dark matter halos in each resolution element (cell of 3³ comoving Mpc³) is determined based on the values of the local density and relative velocity and is derived at each redshift using a modified Press–Schechter model^{114–116}. Gas in dark matter halos above the star formation threshold, parameterized by minimum circular velocity V_c measured in km s⁻¹, are converted into stars with efficiency of f_* .

Given a population of galaxies, radiation fields that interact with the IGM and ultimately determine the strength of the 21-cm signal are calculated as follows. Cosmic heating has several contributions, including X-ray binaries¹¹⁷ (which are the dominant source of heating in most astrophysical cases), Ly- α ^{118,119} and the CMB²⁰. The heating rate by high-redshift X-ray binaries depends on the properties of these sources, most importantly on their efficiency f_x (defined as the ratio of the bolometric X-ray luminosity to star-formation rate) and spectral energy distribution^{60,121–123}, which is modelled as a power-law with a slope α and cutoff frequency ν_{min} . Reionization of the IGM is implemented using the excursion set formalism¹²⁴ and is subject to the photoheating feedback¹²⁵. The process of

reionization is parameterized by the CMB optical depth τ (itself a function of the ionizing efficiency of star-forming galaxies, ζ) and mean free path of ionizing photons R_{mfp} (measured in comoving Mpc).

Additional science outputs. Below we present a list of additional science outputs for the REACH experiment.

- In the case of non-detection, upper limits can be derived on the strength of the absorption feature, which will allow us to put constraints on the astrophysical properties of sources. In particular, if no signal is detected by REACH, that would imply that the signal is either (1) below the detection threshold of the instrument, which would require X-ray sources present before efficient Wouthuysen–Field coupling of the spin and kinetic temperatures of the gas to be very luminous, or (2) outside the REACH band, which would constrain star formation to happening very late and in very massive dark matter halos.
- As illustrated in Fig. 5, a high signal-to-noise detection of the 21-cm signal with REACH will enable us to place competitive independent constraints on τ_{CMB} . In cosmological inference from CMB data, the amplitude of the CMB angular power spectrum is proportional to the degenerate product $A_s e^{-2\tau_{\text{CMB}}}$, where A_s is the amplitude of primordial density fluctuations. Independent constraints on τ_{CMB} break this degeneracy; thus, joint analysis of REACH and Planck data will enable more stringent limits on A_s to be obtained. This, in turn, will enable us to bring into sharper relief current tensions between the A_s inferred using the CMB and directly measured by large-scale structure probes (for example, Sunyaev–Zeldovich cluster counts, galaxy lensing, Baryon acoustic oscillations measurements) on smaller scales (for example, ref. 126). Furthermore, this also would potentially provide science output in inflationary physics, where τ_{CMB} is the only way to get truly closer to cosmic-variance-limited science¹²⁷. We note that the degeneracy between A_s and τ_{CMB} can also be reduced using estimates of τ_{CMB} from large angular-scale modes of CMB polarization power spectra or using CMB lensing, if one assumes no departures from standard Λ cold dark matter model, where Λ is the cosmological constant, cosmology.
- REACH as a gravitational wave detector. It has been postulated¹²⁸ that gravitational waves can be converted into photons in the presence of magnetic fields. This in turn can lead to distortion of the CMB radiation measurable at MHz frequencies with radio telescopes such as REACH. Establishing upper bounds on gravitational waves is therefore a potential high-impact additional science outcome of REACH.
- Better low-frequency sky models constrained by REACH data. The intrinsic joint analysis performed by REACH means that, simultaneously with cosmological models, REACH will produce accurate measurements of foreground model parameters. Therefore, despite its lack of high resolution on the sky, we anticipate important science output from analysing these foreground model fits. Examples include establishing accurate measurements of the spectral index of different large regions of the sky or potential measurements of absolute power of the diffuse emission from the foregrounds.
- Ionosphere and space weather science. REACH is essentially an extremely accurate all-sky (averaged sky) monitor. We expect to be able to use REACH to improve our understanding of the temporal and spectral fluctuations of the large spatial scales of the ionosphere as well as of space weather phenomena (for example, solar activity through its interaction with the ionosphere).
- Serendipitous science. With an extremely accurate and precise radiometer of electromagnetic waves from the sky at long wavelengths (aiming at being the most accurate and precise at frequencies 50–170 MHz), we anticipate the possibility of unexpected discoveries, as is typically the case when technology is pushed to its limits.

Data availability

Upon detection or important scientific result our data will be made publicly available on Zenodo.

Code availability

Upon detection or important scientific result our code will be made publicly available on GitHub. The maxsmooth code can be found online at <https://github.com/htjb/maxsmooth>. The globalemu code can be found online at <https://github.com/htjb/globalemu>.

Received: 29 April 2021; Accepted: 12 May 2022;

Published online: 21 July 2022

References

1. Naoz, S., Noter, S. & Barkana, R. The first stars in the Universe. *Mon. Not. R. Astron. Soc.* **373**, L98–L102 (2006).
2. Loeb, A. & Furlanetto, S. R. *The First Galaxies in the Universe*, Princeton University Press (2013).
3. Klessen, R. in *Formation of the First Black Holes* (eds Latif, M. & Schleicher, D.), World Scientific, 67–97 (2019).
4. Barkana, R. The rise of the first stars: supersonic streaming, radiative feedback, and 21-cm cosmology. *Phys. Rep.* **645**, 1–59 (2016).
5. Furlanetto, S. R., Oh, S. P. & Briggs, F. H. Cosmology at low frequencies: the 21 cm transition and the high-redshift Universe. *Phys. Rep.* **433**, 181–301 (2006).
6. Mesinger, A. *The Cosmic 21-cm Revolution; Charting the First Billion Years of Our Universe*, IOP Science (2019); <https://doi.org/10.1088/2514-3433/ab4a73>
7. Cohen, A., Fialkov, A., Barkana, R. & Lotem, M. Charting the parameter space of the global 21-cm signal. *Mon. Not. R. Astron. Soc.* **472**, 1915–1931 (2017).
8. Fialkov, A., Barkana, R. & Cohen, A. Constraining baryon-dark-matter scattering with the cosmic dawn 21-cm signal. *Phys. Rev. Lett.* **121**, 011101 (2018).
9. Fialkov, A. & Barkana, R. Signature of excess radio background in the 21-cm global signal and power spectrum. *Mon. Not. R. Astron. Soc.* **486**, 1763–1773 (2019).
10. Reis, I., Fialkov, A. & Barkana, R. High-redshift radio galaxies: a potential new source of 21-cm fluctuations. *Mon. Not. R. Astron. Soc.* **499**, 5993–6008 (2020).
11. Bowman, J. D., Rogers, A. E. E. & Hewitt, J. N. Toward empirical constraints on the global redshifted 21 cm brightness temperature during the epoch of reionization. *Astrophys. J.* **676**, 1–9 (2008).
12. Singh, S. et al. SARAS 2 constraints on global 21 cm signals from the epoch of reionization. *Astrophys. J.* **858**, 54 (2018).
13. Philip, L. et al. Probing radio intensity at high- z from Marion: 2017 instrument. *J. Astron. Instrum.* **8**, 1950004 (2019).
14. Bernardi, G. et al. Bayesian constraints on the global 21-cm signal from the cosmic dawn. *Mon. Not. R. Astron. Soc.* **461**, 2847–2855 (2016).
15. Voytek, T. C., Natarajan, A., Jáuregui García, J. M., Peterson, J. B. & López-Cruz, O. Probing the dark ages at $z \sim 20$: the SCI-H 1 21 cm all-sky spectrum experiment. *Astrophys. J. Lett.* **782**, L9 (2014).
16. Sokolowski, M. et al. BIGHORNS - broadband instrument for global hydrogen reionisation signal. *Publ. Astron. Soc. Aust.* **32**, e004 (2015).
17. Bowman, J. D., Rogers, A. E. E., Monsalve, R. A., Mozdzen, T. J. & Mahesh, N. An absorption profile centred at 78 megahertz in the sky-averaged spectrum. *Nature* **555**, 67–70 (2018).
18. Mirocha, J. & Furlanetto, S. R. What does the first highly redshifted 21-cm detection tell us about early galaxies? *Mon. Not. R. Astron. Soc.* **483**, 1980–1992 (2019).
19. Schauer, A. T. P., Liu, B. & Bromm, V. Constraining first star formation with 21 cm cosmology. *Astrophys. J. Lett.* **877**, L5 (2019).
20. Cohen, A., Fialkov, A., Barkana, R. & Lotem, M. Charting the parameter space of the global 21-cm signal. *Mon. Not. R. Astron. Soc.* **472**, 1915–1931 (2017).
21. Cohen, A., Fialkov, A., Barkana, R. & Monsalve, R. A. Emulating the global 21-cm signal from cosmic dawn and reionization. *Mon. Not. R. Astron. Soc.* **495**, 4845–4859 (2020).
22. Reis, I., Fialkov, A. & Barkana, R. The subtlety of Ly- α photons: changing the expected range of the 21-cm signal. Preprint at <https://arxiv.org/abs/2101.01777> (2021).
23. Furlanetto, S. R. & Pritchard, J. R. The scattering of Lyman-series photons in the intergalactic medium. *Mon. Not. R. Astron. Soc.* **372**, 1093–1103 (2006).
24. Pritchard, J. R. & Furlanetto, S. R. Descending from on high: Lyman-series cascades and spin-kinetic temperature coupling in the 21-cm line. *Mon. Not. R. Astron. Soc.* **367**, 1057–1066 (2006).
25. Wouthuysen, S. A. On the excitation mechanism of the 21-cm (radio-frequency) interstellar hydrogen emission line. *Astron. J.* **57**, 31–32 (1952).
26. Field, G. B. Excitation of the hydrogen 21-cm line. *Proc. IRE* **46**, 240–250 (1958).
27. Hills, R., Kulkarni, G., Meerburg, P. D. & Puchwein, E. Concerns about modelling of the EDGES data. *Nature* **564**, E32–E34 (2018).
28. Singh, S. & Subrahmanyan, R. The redshifted 21 cm signal in the EDGES low-band spectrum. *Astrophys. J.* **880**, 26 (2019).
29. Sims, P. H. & Pober, J. C. Testing for calibration systematics in the EDGES low-band data using Bayesian model selection. *Mon. Not. R. Astron. Soc.* **492**, 22–38 (2020).
30. Bevins, H. T. J. et al. maxsmooth: rapid maximally smooth function fitting with applications in global 21-cm cosmology. *Mon. Not. R. Astron. Soc.* **502**, 4405–4425 (2021).
31. Singh, S. et al. On the detection of a cosmic dawn signal in the radio background. *Nat. Astron.* **6**, 607–617 (2022).
32. Handley, W. J., Hobson, M. P. & Lasenby, A. N. POLYCHORD: next-generation nested sampling. *Mon. Not. R. Astron. Soc.* **453**, 4384–4398 (2015).
33. Handley, W. J., Hobson, M. P. & Lasenby, A. N. polychord: nested sampling for cosmology. *Mon. Not. R. Astron. Soc.* **450**, L61–L65 (2015).

34. Dewdney, P. E., Hall, P. J., Schilizzi, R. T. & Lazio, T. J. L. W. The Square Kilometre Array. *Proc. IEEE* **97**, 1482–1496 (2009).
35. Jonas, J. L. Meerkat—the South African array with composite dishes and wide-band single pixel feeds. *Proceedings of the IEEE* **97**, 1522–1530 (2009).
36. DeBoer, D. R. et al. Hydrogen Epoch of Reionization Array (HERA). *Publ. Astron. Soc. Pac.* **129**, 045001 (2017).
37. Anstey, D., de Lera Acedo, E. & Handley, W. A general Bayesian framework for foreground modelling and chromaticity correction for global 21cm experiments. *Mon. Not. R. Astron. Soc.* <https://doi.org/10.1093/mnras/stab1765> (2021).
38. Roque, I. L. V., Handley, W. J. & Razavi-Ghods, N. Bayesian noise wave calibration for 21-cm global experiments. *Mon. Not. R. Astron. Soc.* **505**, 2638–2646 (2021).
39. Anstey, D., Cumner, J., de Lera Acedo, E. & Handley, W. Informing antenna design for sky-averaged 21-cm experiments using a simulated Bayesian data analysis pipeline. *Mon. Not. R. Astron. Soc.* **509**, 4679–4693 (2021).
40. Cumner, J. et al. Radio antenna design for sky-averaged 21cm cosmology experiments: the reach case. *J. Astron. Instrum.* **11**, 2250001 (2022).
41. Shen, E., Anstey, D., de Lera Acedo, E., Fialkov, A. & Handley, W. Quantifying ionospheric effects on global 21-cm observations. *Mon. Not. R. Astron. Soc.* **503**, 344–353 (2021).
42. Bevins, H. T. J., Handley, W. J., Fialkov, A., de Lera Acedo, E. & Javid, K. GLOBALEMU: a novel and robust approach for emulating the sky-averaged 21-cm signal from the cosmic dawn and epoch of reionization. *Mon. Not. R. Astron. Soc.* **508**, 2923–2936 (2021).
43. Scheutwinkel, K. H., Handley, W. & de Lera Acedo, E. Bayesian evidence-driven likelihood selection for sky-averaged 21-cm signal extraction. Preprint at <https://arxiv.org/abs/2204.04491> (2022).
44. Scheutwinkel, K. H., de Lera Acedo, E. & Handley, W. Bayesian evidence-driven diagnosis of instrumental systematics for sky-averaged 21-cm cosmology experiments. Preprint at <https://arxiv.org/abs/2204.04445> (2022).
45. Rao, M. S., Subrahmanyam, R., Shankar, N. U. & Chluba, J. Modeling the radio foreground for detection of CMB spectral distortions from the cosmic dawn and the epoch of reionization. *Astrophys. J.* **840**, 33 (2017).
46. Rogers, A. E. E. & Bowman, J. D. Spectral index of the diffuse radio background measured from 100 to 200 MHz. *Astron. J.* **136**, 641–648 (2008).
47. Singh, S. et al. SARAS 2: a spectral radiometer for probing cosmic dawn and the epoch of reionization through detection of the global 21-cm signal. *Exp. Astron.* **45**, 269–314 (2018).
48. Price, D. C. et al. Design and characterization of the Large-aperture Experiment to Detect the Dark Age (LEDA) radiometer systems. *Mon. Not. R. Astron. Soc.* **478**, 4193–4213 (2018).
49. Rogers, A. E. E. & Bowman, J. D. Absolute calibration of a wideband antenna and spectrometer for accurate sky noise temperature measurements. *Radio Sci.* **47**, RS0K06 (2012).
50. Feng, C. & Holder, G. Enhanced global signal of neutral hydrogen due to excess radiation at cosmic dawn. *Astrophys. J. Lett.* **858**, L17 (2018).
51. Ewall-Wice, A. et al. Modeling the radio background from the first black holes at cosmic dawn: implications for the 21 cm absorption amplitude. *Astrophys. J.* **868**, 63 (2018).
52. Brandenberger, R., Cyr, B. & Shi, R. Constraints on superconducting cosmic strings from the global 21-cm signal before reionization. *J. Cosmol. Astropart. Phys.* **2019**, 009 (2019).
53. Ewall-Wice, A., Chang, T.-C. & Lazio, T. J. W. The radio scream from black holes at cosmic dawn: a semi-analytic model for the impact of radio-loud black holes on the 21 cm global signal. *Mon. Not. R. Astron. Soc.* **492**, 6086 (2020).
54. Barkana, R. Possible interaction between baryons and dark-matter particles revealed by the first stars. *Nature* **555**, 71–74 (2018).
55. Berlin, A., Hooper, D., Krnjaic, G. & McDermott, S. D. Severely constraining dark-matter interpretations of the 21-cm anomaly. *Phys. Rev. Lett.* **121**, 011102 (2018).
56. Barkana, R., Outmezguine, N. J., Redigol, D. & Volansky, T. Strong constraints on light dark matter interpretation of the EDGES signal. *Phys. Rev. D* **98**, 103005 (2018).
57. Muñoz, J. B. & Loeb, A. A small amount of mini-charged dark matter could cool the baryons in the early Universe. *Nature* **557**, 684–686 (2018).
58. Liu, H., Outmezguine, N. J., Redigolo, D. & Volansky, T. Reviving millicharged dark matter for 21-cm cosmology. *Phys. Rev. D* **100**, 123011 (2019).
59. Visbal, E., Barkana, R., Fialkov, A., Tselikhovich, D. & Hirata, C. M. The signature of the first stars in atomic hydrogen at redshift 20. *Nature* **487**, 70–73 (2012).
60. Fialkov, A. & Barkana, R. The rich complexity of 21-cm fluctuations produced by the first stars. *Mon. Not. R. Astron. Soc.* **445**, 213–224 (2014).
61. Mirocha, J. Decoding the X-ray properties of pre-reionization era sources. *Mon. Not. R. Astron. Soc.* **443**, 1211–1223 (2014).
62. Fixsen, D. J. et al. ARCADE 2 measurement of the absolute sky brightness at 3–90 GHz. *Astrophys. J.* **734**, 5 (2011).
63. Dowell, J. & Taylor, G. B. The radio background below 100 MHz. *Astrophys. J. Lett.* **858**, L9 (2018).
64. Urry, C. M. & Padovani, P. Unified schemes for radio-loud active galactic nuclei. *Publ. Astron. Soc. Pac.* **107**, 803 (1995).
65. Biermann, P. L. et al. Cosmic backgrounds due to the formation of the first generation of supermassive black holes. *Mon. Not. R. Astron. Soc.* **441**, 1147–1156 (2014).
66. Bolgar, F., Eames, E., Hottier, C. & Semelin, B. Imprints of quasar duty cycle on the 21-cm signal from the epoch of reionization. *Mon. Not. R. Astron. Soc.* **478**, 5564–5578 (2018).
67. Condon, J. J. Radio emission from normal galaxies. *Annu. Rev. Astron. Astrophys.* **30**, 575–611 (1992).
68. Jana, R., Nath, B. B. & Biermann, P. L. Radio background and IGM heating due to Pop III supernova explosions. *Mon. Not. R. Astron. Soc.* **483**, 5329–5333 (2019).
69. Bolliet, B., Chluba, J. & Battye, R. Spectral distortion constraints on photon injection from low-mass decaying particles. *Mon. Not. R. Astron. Soc.* **507**, 3148–3178 (2021).
70. Brahma, N., Sethi, S. & Sista, S. Energy injection in pre-recombination era and EDGES detection. *J. Cosmol. Astropart. Phys.* **2020**, 034 (2020).
71. Fraser, S. et al. The EDGES 21 cm anomaly and properties of dark matter. *Phys. Lett. B* **785**, 159–164 (2018).
72. Pospelov, M., Pradler, J., Ruderman, J. T. & Urbano, A. Room for new physics in the Rayleigh–Jeans tail of the cosmic microwave background. *Phys. Rev. Lett.* **121**, 031103 (2018).
73. Caputo, A. et al. Edges and endpoints in 21-cm observations from resonant photon production. *Phys. Rev. Lett.* **127**, 011102 (2021).
74. Dhuria, M., Karambelkar, V., Rental, V. & Sarmah, P. A strong broadband 21 cm cosmological signal from dark matter spin-flip interactions. *J. Cosmol. Astropart. Phys.* **2021**, 041 (2021).
75. Mozdzen, T. J., Bowman, J. D., Monsalve, R. A. & Rogers, A. E. E. Improved measurement of the spectral index of the diffuse radio background between 90 and 190 MHz. *Mon. Not. R. Astron. Soc.* **464**, 4995–5002 (2017).
76. Mozdzen, T. J., Mahesh, N., Monsalve, R. A., Rogers, A. E. E. & Bowman, J. D. Spectral index of the diffuse radio background between 50 and 100 MHz. *Mon. Not. R. Astron. Soc.* **483**, 4411–4423 (2018).
77. Meys, R. P. A wave approach to the noise properties of linear microwave devices. *IEEE Trans. Microw. Theory Tech.* **MTT- 26**, 34–37 (1978).
78. Dicke, R. H. The measurement of thermal radiation at microwave frequencies. *Rev. Sci. Instrum.* **17**, 106–113 (1946).
79. Monsalve, R. A., Rogers, A. E. E., Bowman, J. D. & Mozdzen, T. J. Calibration of the EDGES high-band receiver to observe the global 21 cm signature from the epoch of reionization. *Astrophys. J.* **835**, 49 (2017).
80. Waterson, M. F. et al. The SKA1 LOW telescope: system architecture and design performance. In *Society of Photo-Optical Instrumentation Engineers (SPIE) Conference Series*, Vol. 9906 (eds Hall, H. J. et al.) 798–811 (SPIE, 2016); <https://doi.org/10.1117/12.2232526>
81. Naldi, G. et al. The digital signal processing platform for the low frequency aperture array: preliminary results on the data acquisition unit. *J. Astron. Instrum.* **06**, 1641014 (2017).
82. Melis, A. et al. A digital beamformer for the PHAROS2 phased array feed. *J. Astron. Instrum.* **09**, 2050013 (2020).
83. Locatelli, N. T. et al. The Northern Cross fast radio burst project. I. Overview and pilot observations at 408 MHz. *Mon. Not. R. Astron. Soc.* **494**, 1229–1236 (2020).
84. Magro, A. et al. A new digital backend for the Mexican Array Radio Telescope. In *2019 International Conference on Electromagnetics in Advanced Applications* 0185–0189 (IEEE, 2019); <https://doi.org/10.1109/ICEAA.2019.8878959>
85. Magro, A. et al. A software infrastructure for firmware-software interaction: the case of TPMs. In *2017 International Conference on Signals and Systems* 190–196 (IEEE, 2017); <https://doi.org/10.1109/ICSSIGSYS.2017.7967039>
86. Josaitis, A. & de Lera Acedo, E. *Measurements of the Radio Spectrum from 10–240 MHz in the SKA-SA Core Site* (2019); <https://tinyurl.com/3efjednb>
87. Newburgh, L. B. et al. HIRAX: a probe of dark energy and radio transients. In *Society of Photo-Optical Instrumentation Engineers (SPIE) Conference Series*, Vol. 9906 (eds Hall, H. J. et al.) 99065X (SPIE, 2016); <https://doi.org/10.1117/12.2234286>
88. de Lera Acedo, E. et al. SKA aperture array verification system: electromagnetic modeling and beam pattern measurements using a micro UAV. *Exp. Astron.* **45**, 1–20 (2018).
89. Cavillot, J., Tihon, D., Mesa, F., de Lera Acedo, E. & Craeye, C. Efficient simulation of large irregular arrays on a finite ground plane. *IEEE Trans. Antennas Propag.* **68**, 2753–2764 (2020).
90. Handley, W. J., Lasenby, A. N., Peiris, H. V. & Hobson, M. P. Bayesian inflationary reconstructions from Planck 2018 data. *Phys. Rev. D* **100**, 103511 (2019).

91. Skilling, J. Nested sampling for general Bayesian computation. *Bayesian Anal.* **1**, 833–859 (2006).
92. Hergt, L. T., Handley, W. J., Hobson, M. P. & Lasenby, A. N. Bayesian evidence for the tensor-to-scalar ratio r and neutrino masses m_ν : effects of uniform versus logarithmic priors. *Phys. Rev. D* **103**, 123511 (2021).
93. Shaver, P. A., Windhorst, R. A., Madau, P. & de Bruyn, A. G. Can the reionization epoch be detected as a global signature in the cosmic background? *Astron. Astrophys.* **345**, 380–390 (1999).
94. Pritchard, J. & Loeb, A. Cosmology: hydrogen was not ionized abruptly. *Nature* **468**, 772–773 (2010).
95. Bowman, J. D. & Rogers, A. E. E. A lower limit of $\Delta z > 0.06$ for the duration of the reionization epoch. *Nature* **468**, 796–798 (2010).
96. Presley, M. E., Liu, A. & Parsons, A. R. Measuring the cosmological 21 cm monopole with an interferometer. *Astrophys. J.* **809**, 18 (2015).
97. Bernardi, G., McQuinn, M. & Greenhill, L. J. Foreground model and antenna calibration errors in the measurement of the sky-averaged $\lambda 21$ cm signal at $z \sim 20$. *Astrophys. J.* **799**, 90 (2015).
98. Sathyanarayana Rao, M., Subrahmanyan, R., Udaya Shankar, N. & Chluba, J. GMOSS: all-sky model of spectral radio brightness based on physical components and associated radiative processes. *Astron. J.* **153**, 26 (2017).
99. Singh, S. et al. First results on the epoch of reionization from first light with SARAS 2. *Astrophys. J. Lett.* **845**, L12 (2017).
100. Nhan, B. D., Bradley, R. F. & Burns, J. O. A polarimetric approach for constraining the dynamic foreground spectrum for cosmological global 21 cm measurements. *Astrophys. J.* **836**, 90 (2017).
101. Monsalve, R. A., Rogers, A. E. E., Bowman, J. D. & Mozdzen, T. J. Results from EDGES high-band. I. Constraints on phenomenological models for the global 21 cm signal. *Astrophys. J.* **847**, 64 (2017).
102. Monsalve, R. A. et al. Results from EDGES high-band. II. Constraints on parameters of early galaxies. *Astrophys. J.* **863**, 11 (2018).
103. Monsalve, R. A. et al. Results from EDGES high-band. III. New constraints on parameters of the early Universe. *Astrophys. J.* **875**, 67 (2019).
104. Tauscher, K., Rapetti, D., Burns, J. O. & Switzer, E. Global 21 cm signal extraction from foreground and instrumental effects. I. Pattern recognition framework for separation using training sets. *Astrophys. J.* **853**, 187 (2018).
105. Rapetti, D., Tauscher, K., Mirocha, J. & Burns, J. O. Global 21 cm signal extraction from foreground and instrumental effects. II. Efficient and self-consistent technique for constraining nonlinear signal models. *Astrophys. J.* **897**, 174 (2020).
106. Hibbard, J. J., Tauscher, K., Rapetti, D. & Burns, J. O. Modeling the Galactic foreground and beam chromaticity for global 21 cm cosmology. *Astrophys. J.* **905**, 113 (2020).
107. De Oliveira-Costa, A. et al. A model of diffuse Galactic radio emission from 10 MHz to 100 GHz. *Mon. Not. R. Astron. Soc.* **388**, 247–260 (2008).
108. Guzmán, A. E., May, J., Alvarez, H. & Maeda, K. All-sky Galactic radiation at 45 MHz and spectral index between 45 and 408 MHz. *Astron. Astrophys.* **525**, A138 (2011).
109. Patra, N., Subrahmanyan, R., Sethi, S., Shankar, N. U. & Raghunathan, A. SARAS measurement of the radio background at long wavelengths. *Astrophys. J.* **801**, 138 (2015).
110. Spinelli, M. et al. Spectral index of the Galactic foreground emission in the 50–87 MHz range. *Mon. Not. R. Astron. Soc.* **505**, 1575–1588 (2021).
111. Spinelli, M., Bernardi, G. & Santos, M. G. On the contamination of the global 21-cm signal from polarized foregrounds. *Mon. Not. R. Astron. Soc.* **489**, 4007–4015 (2019).
112. Bevins, H. T. J. maxsmooth: derivative constrained function fitting. *J. Open Source Softw.* **5**, 2596 (2020).
113. Tseliakhovich, D. & Hirata, C. Relative velocity of dark matter and baryonic fluids and the formation of the first structures. *Phys. Rev. D* **82**, 083520 (2010).
114. Press, W. H. & Schechter, P. Formation of galaxies and clusters of galaxies by self-similar gravitational condensation. *Astrophys. J.* **187**, 425–438 (1974).
115. Sheth, R. K. & Tormen, G. Large-scale bias and the peak background split. *Mon. Not. R. Astron. Soc.* **308**, 119–126 (1999).
116. Barkana, R. & Loeb, A. Unusually large fluctuations in the statistics of galaxy formation at high redshift. *Astrophys. J.* **609**, 474–481 (2004).
117. Fragos, T. et al. X-ray binary evolution across cosmic time. *Astrophys. J.* **764**, 41 (2013).
118. Chuzhoy, L. & Shapiro, P. R. Heating and cooling of the early intergalactic medium by resonance photons. *Astrophys. J.* **655**, 843–846 (2007).
119. Mittal, S. & Kulkarni, G. Ly α coupling and heating at cosmic dawn. *Mon. Not. R. Astron. Soc.* **503**, 4264–4275 (2020).
120. Venumadhav, T., Dai, L., Kaurav, A. & Zaldarriaga, M. Heating of the intergalactic medium by the cosmic microwave background during cosmic dawn. *Phys. Rev. D* **98**, 103513 (2018).
121. Fialkov, A., Barkana, R. & Visbal, E. The observable signature of late heating of the Universe during cosmic reionization. *Nature* **506**, 197–199 (2014).
122. Pacucci, F., Mesinger, A., Mineo, S. & Ferrara, A. The X-ray spectra of the first galaxies: 21 cm signatures. *Mon. Not. R. Astron. Soc.* **443**, 678–686 (2014).
123. Cohen, A., Fialkov, A. & Barkana, R. Charting the parameter space of the 21-cm power spectrum. *Mon. Not. R. Astron. Soc.* **478**, 2193–2217 (2018).
124. Furlanetto, S. R., Zaldarriaga, M. & Hernquist, L. The growth of H II regions during reionization. *Astrophys. J.* **613**, 1–15 (2004).
125. Cohen, A., Fialkov, A. & Barkana, R. The 21-cm BAO signature of enriched low-mass galaxies during cosmic reionization. *Mon. Not. R. Astron. Soc.* **459**, L90–L94 (2016).
126. Batty, R. A., Charnock, T. & Moss, A. Tension between the power spectrum of density perturbations measured on large and small scales. *Phys. Rev. D* **91**, 103508 (2015).
127. Finelli, F. et al. Exploring cosmic origins with CORE: inflation. *J. Cosmol. Astropart. Phys.* **2018**, 016 (2018).
128. Domcke, V. & Garcia-Cely, C. Potential of radio telescopes as high-frequency gravitational wave detectors. *Phys. Rev. Lett.* **126**, 021104 (2021).

Acknowledgements

The REACH collaboration acknowledges the Kavli Institute for Cosmology in Cambridge (www.kicc.cam.ac.uk), Stellenbosch University (www.sun.ac.za), the National Research Foundation of South Africa (www.nrf.ac.za) and the Cambridge–Africa ALBORADA Research Fund (www.cambridge-africa.cam.ac.uk/initiatives/the-alborada-research-fund/) for their financial support of the project. E.d.L.A. wishes to acknowledge the support of the Science and Technology Facilities Council (STFC) through grant number ST/V004425/1 (Ernest Rutherford Fellowship). G.B. and M.S. acknowledge support from the Ministero degli Affari Esteri della Cooperazione Internazionale–Direzione Generale per la Promozione del Sistema Paese Progetto di Grande Rilevanza ZA18GR02 and the National Research Foundation of South Africa (Grant Number 113121) as part of the ISARP RADIOSKY2020 Joint Research Scheme. The research of D.I.L.d.V. and O.S. is supported by the South African Research Chairs Initiative of the Department of Science and Technology and National Research Foundation. M.S. acknowledges funding from the INAF PRIN-SKA 2017 project 1.05.01.88.04 (FORECAST). This work is based on the research supported in part by the National Research Foundation of South Africa (Grant Number 75322). H.T.J.B. acknowledges the support of the STFC through grant number ST/T505997/1.

Author contributions

E.d.L.A. is the PI and initiator of REACH and led the coordination of the paper write-up and the ‘Main’, ‘Experimental approach’, ‘System design’, ‘High-level system metrics’, ‘Data analysis pipeline’ and ‘Instrument models’ sections. D.I.L.d.V. is the co-PI of REACH and led the ‘Antennas’ and ‘Site and RFI’ sections. N.R.-G. led the ‘Receiver and calibrator’ section. W.H. led the ‘Bayesian data analysis and calibration’ section. A.F. co-led the ‘Science prospects’ section, led the ‘Cosmological models’ section and contributed to the ‘Main’ section. A.M. led the ‘Digital back-end’ section. D.A. led the ‘EDGES data re-analysis’, ‘Data-analysis-driven antenna selection’, ‘Foreground models and chromaticity correction’ and ‘Time- and antenna-dependent modelling’ sections. H.T.J.B. led the ‘Detection of systematic errors’ section. R.C. contributed notably to the ‘Digital back-end’ section. J. Cumner contributed notably to the ‘Antennas’ section. A.T.J. contributed notably to the ‘Site and RFI’ section. I.L.V.R. led the ‘Bayesian receiver calibration’ section. P.H.S. co-led the ‘Science prospects’ section. K.H.S. led the ‘Systematic signals in the data pipeline’ section. The rest of the authors (P.A., G.B., S.C., J. Cavillot, W.C., J.A.E., T.G.-J., Q.G., R.H., G.K., R.M., P.D.M., S.M., J.R.P., E.P., A.S., E.S., O.S., M.S. and K.Z.-A.) contributed to writing different sections and to reviewing the manuscript.

Competing interests

The authors declare no competing interests.

Additional information

Extended data is available for this paper at <https://doi.org/10.1038/s41550-022-01709-9>.

Supplementary information The online version contains supplementary material available at <https://doi.org/10.1038/s41550-022-01709-9>.

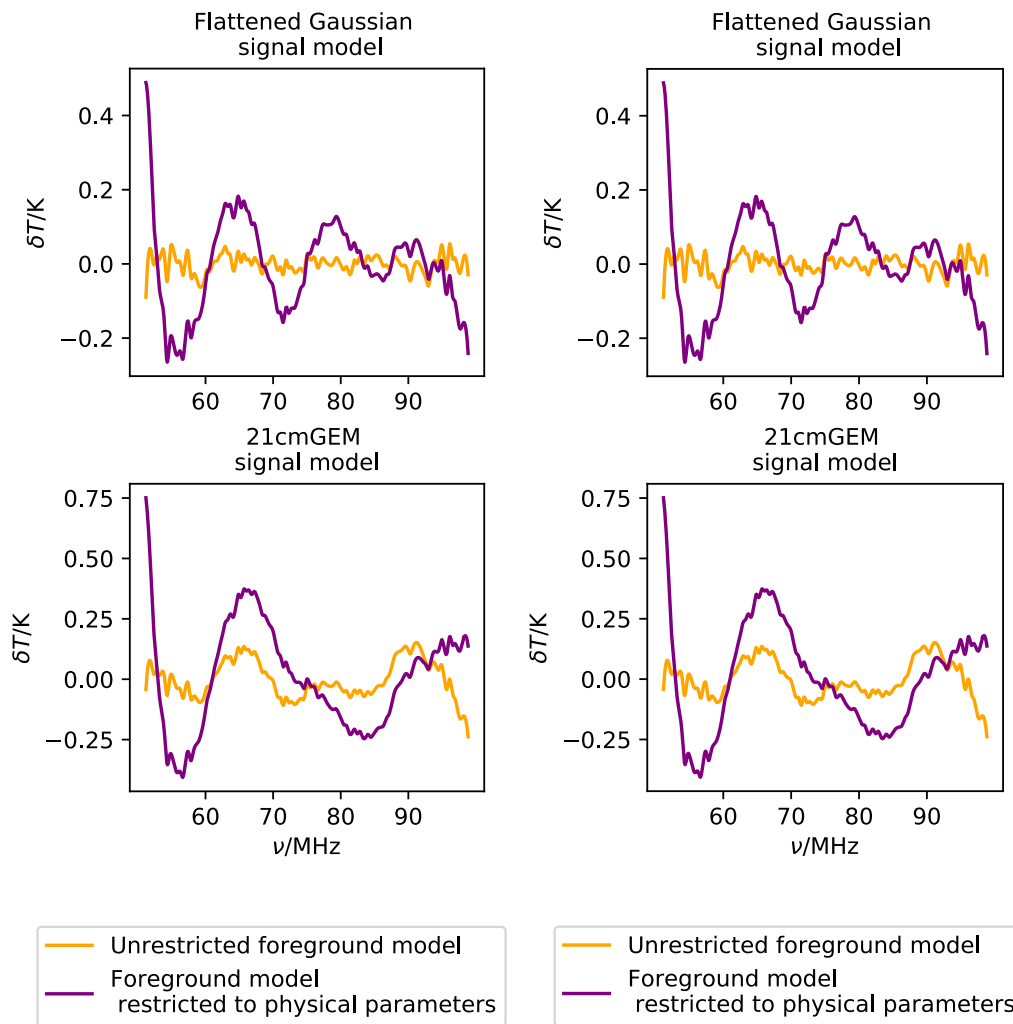
Correspondence and requests for materials should be addressed to E. de Lera Acedo.

Peer review information *Nature Astronomy* thanks the anonymous reviewers for their contribution to the peer review of this work.

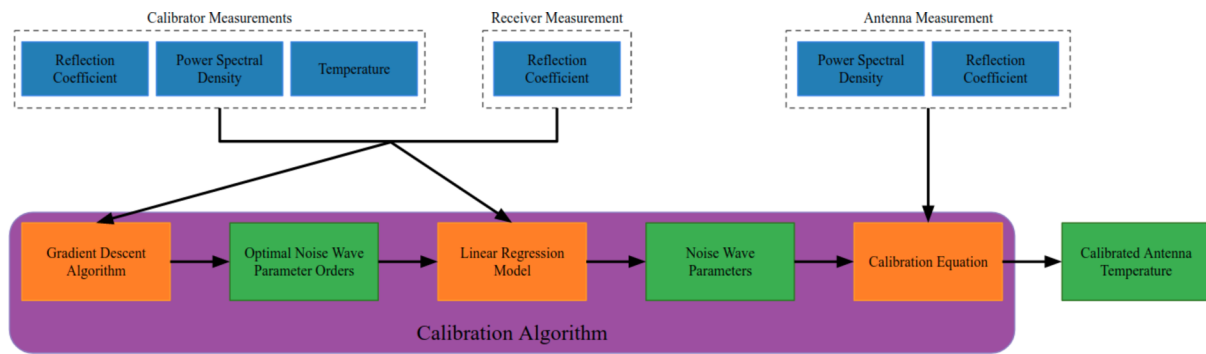
Reprints and permissions information is available at www.nature.com/reprints.

Publisher’s note Springer Nature remains neutral with regard to jurisdictional claims in published maps and institutional affiliations.

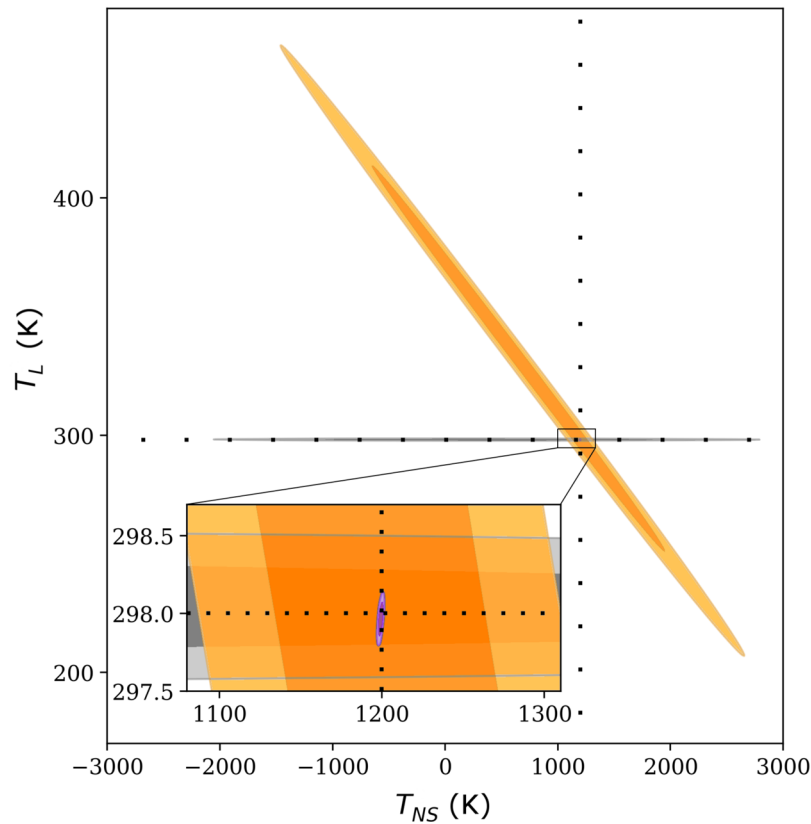
© The Author(s), under exclusive licence to Springer Nature Limited 2022



Extended Data Fig. 1 | Re-analysis of EDGES public data. Re-analysis of the publicly available EDGES data restricting the foregrounds to physical parameters (purple) and with unrestricted foreground parameters (orange) for a flattened Gaussian EDGES-style signal model (top-left) and a 21cmGEM standard physical model from [20] (bottom-left). On the right column we show the corresponding residuals after subtraction of the posterior average fitted foreground and signal models.

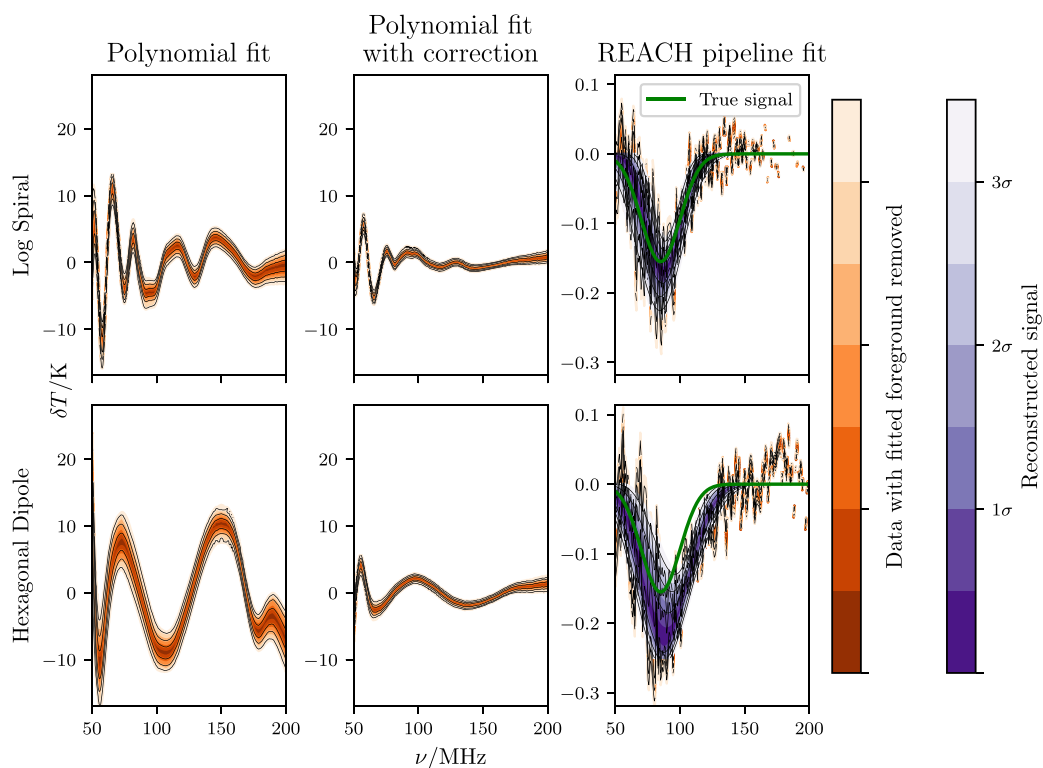
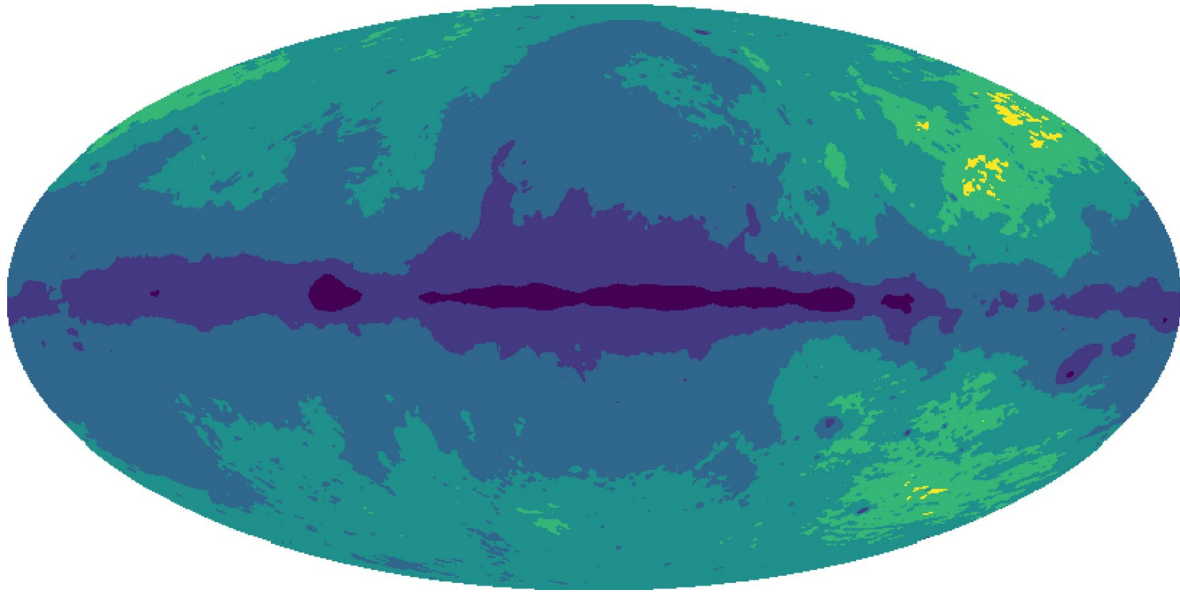


■ cold load ■ hot load ■ cold load + hot load

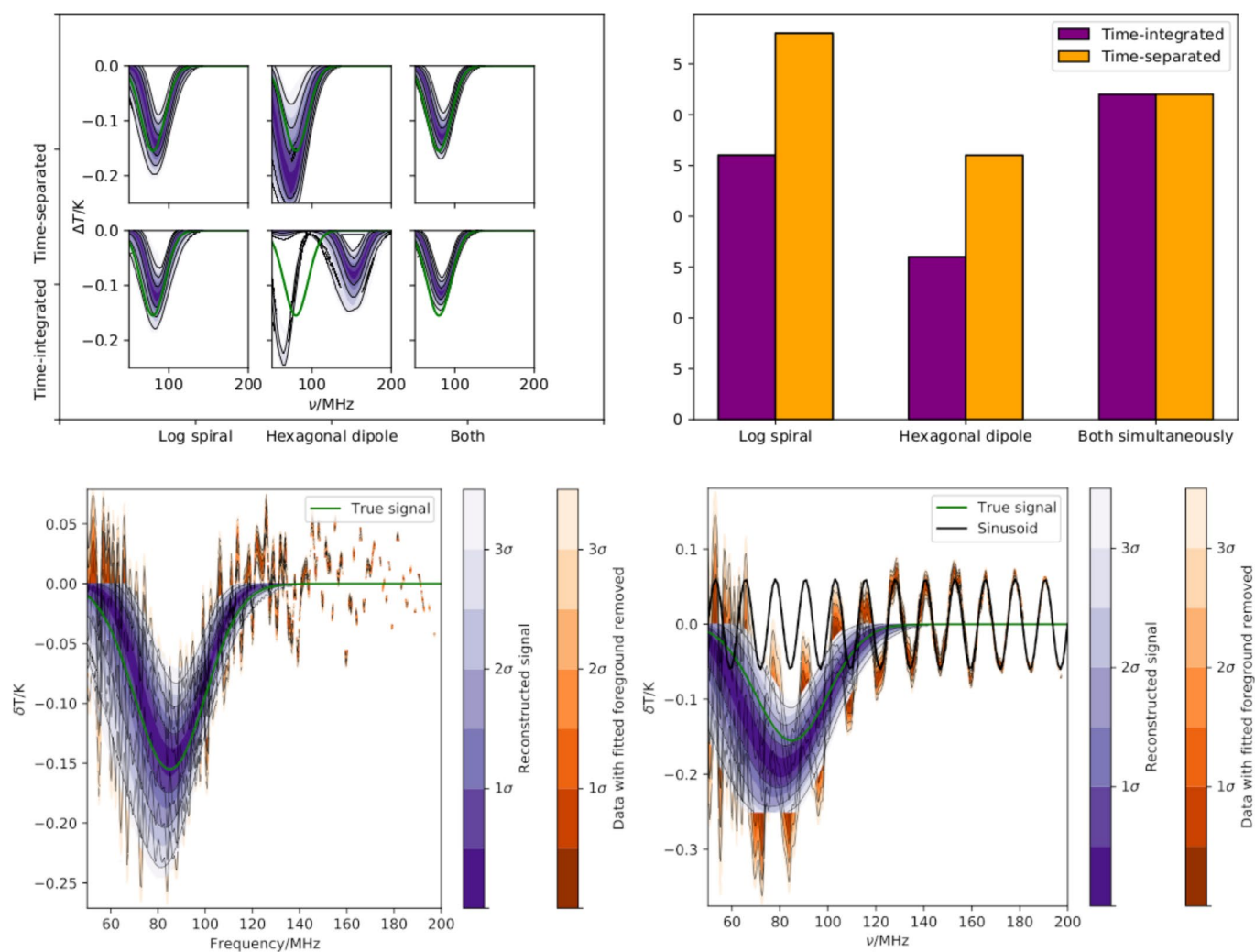


Extended Data Fig. 2 | REACH RX calibration. Top: Outline of the calibration algorithm. Blue blocks represent data to be taken, red blocks represent calculations and green blocks represent calculation outputs. Bottom: Plot showing the joint posteriors for two noise wave parameters used for calibration of the receiver; T_L and T_{NS} . Posteriors are derived using a single room-temperature ‘cold’ load as a calibrator, a single ‘hot’ load heated to 373 K and both loads used in tandem shown in grey, red and blue respectively. The black cross hairs mark the known values of the calibration parameters. A zoom-in of the posterior intersection is provided to illustrate the constraint on parameter values attributed to the correlation between parameters that is considered by our algorithm when deriving the blue, dual-load posterior.

6 Regions



Extended Data Fig. 3 | Foreground modelling. Top: Plot showing the subdivision of the sky in galactic coordinates into a number of regions $N=6$ of similar spectral index. Bottom: Plot comparing the residuals from fitting simulated 21-cm data. The plots show the results of fitting data with a 5th order log-polynomial model (left), fitting data corrected by (A1) with a 5th order log-polynomial model (centre) and fitting the data with the REACH pipeline, using $N=9$ (right). The residuals after subtraction of the foreground models are shown in red. The signal model and true signal inserted into the simulated data, are shown in blue and green respectively, where visible. These results are simulated using a conical log-spiral antenna and a hexagonal dipole antenna.



Extended Data Fig. 4 | Resilience to systematic signals. Top-left: Plot of the recovered 21-cm signal in purple, compared to the true inserted 21-cm signal in green, for simulated data sets of a log spiral and hexagonal dipole antenna. Each data set consisted of three time bins, 20 minutes apart. The lower plots show the results of fitting an integration of the three bins to a single foreground model and the upper plots show the results of fitting the separate bins jointly to corresponding models in a single fit. The rightmost plots show the results of fitting the data sets from both antenna simultaneously in the same fit. Top-right: Plot of the optimum numbers of foreground regions, determined using the Bayesian evidence, for the model fits shown in the top-left plot. Bottom-left: Plot showing a run of the pipeline where the antenna model included the presence of the finite 20x20 m metallic ground plane underneath the spiral antenna. This plot shows that the chromaticity introduced by reflections at the edge of the REACH ground plane, if properly modelled, would not severely affect the ability of the pipeline to recover the cosmological signal. Bottom-right: Plot showing the result of running the data pipeline when a sinusoidal systematic arising from the presence of the 6 m cable connecting the spiral antenna feed point to the receiver has been introduced in the data. The additive systematic signal is shown as a black-solid line in this plot. In the simulated analysis we included a sinusoidal model to fit for this systematic signal simultaneously with the foregrounds and the cosmological signal. This result shows that a detection of the true signal could be achieved in this case.